Discrimination and Enhancement of Fracture Signals on Surface Seismic Data

Reeshidev Bansal

Thesis submitted to the faculty of Virginia Polytechnic Institute and State University in partial fulfillment of the requirements for the degree of

Master of Science
in
Geological Science

Dr. Matthias G. Imhof, Chair

Dr. John A. Hole **Dr. Cahit Coruh**

May 5th, 2003
Blacksburg, Virginia

Keywords: Fractures, Gas Reservoirs, Seismic Data Processing

Discrimination and Enhancement of Fracture Signals on Surface Seismic Data

Reeshidev Bansal

Abstract

Fracture patterns control flow and transport properties in a tight gas reservoir and therefore play a great role in siting the production wells. Hence, it is very important that the exact location and orientation of fractures or fracture swarms are known. Numerical models show that the fractures may be manifested on seismograms as discrete events. A number of data processing workflows were designed and examined to enhance these fracture signals and to suppress the reflections from layer boundaries in seismic data. The workflows were first tested on a 2D synthetic data set, and then applied to 3D field data from the San Juan Basin in New Mexico.

All these workflows combine conventional processing tools which makes them easily applicable. Use of conventional P-wave data may also make this approach to locate fractures more economical than other currently available technology which often requires acquisition and processing of S-wave survey or computationally intensive inversion of data.

Diode filtering and dip-filtering in the common-offset domain yield good results and work very well in the presence of flat reflectors. NMO-Dip filter depends on the NMO velocity of the subsurface, but removes both flat and slightly dipping reflectors without affecting the fracture signals. Prior application of dip-moveout correction (DMO) did not make any difference on reflections, but included some incoherent noise to the data. The

Eigenvector filter performed very well on flat or near-flat reflectors and left the fracture signals almost intact, but introduced some incoherent noise in the presence of steeply dipping reflectors. Harlan's scheme and Radon filtering are very sensitive with regard to parameters selection, but perform exceptionally well on flat or near-flat reflectors.

Dip-filter, Eigenvector filter, and Radon filter were also tested on 3D land data. Dip-filter and Eigenvector filter suppressed strong reflections with slight perturbations to the fracture signals. Radon filter did not produce satisfactory result due to small residual moveout difference between reflectors and fracture signals.

Acknowledgments

First, I would like to thank my adviser, Dr. Matthias G. Imhof for bearing with me for these two years, and for providing a constant source of knowledge and inspiration. I also wish to thank the faculty members at the Department of Geological Sciences and all my fellow student at Geophysics Graduate Students office.

I thank Dr. Cahit Coruh and Dr. John A. Hole for serving on my committee, and for giving me invaluable suggestions and feedback on my work. Their help was crucial during the last stage of preparing my thesis.

I wish to thank Tom Daley from Lawrence Berkeley National Laboratory (LBNL) for letting me use his results in my thesis.

This work is part of the "Development and Validation of the Next Generation Method for Quantifying Naturally Fractured Gas Reservoirs" in collaboration with the Department of Energy, Lawrence Berkeley National Laboratory, ConocoPhilips, Schlumberger, and Stanford University. The project is supported by the Assistant Secretary for Fossil Energy, National Energy Technology Laboratory (NETL). I would like to thank NETL project managers Thomas Mroz and Frances Toro for their financial support.

Reeshidev Bansal
Blacksburg, April-2003

Table of Contents

Introduction

Rocks in tight gas reservoirs are often characterized by sufficient porosity, but very low matrix permeability (<0.1 mD) which might render gas production unprofitable. This type of reservoir, however, is often rich in fractures which provide the necessary open channels for the flow of gas, and may even control the permeability of the reservoir (Durrast et al., 2002). A high density of naturally occurring fractures has been recognized as a controlling factor for commercial success of production wells (PTTC, 1999).

In addition to simple permeability enhancement, fractures in tight gas sand also introduce anisotropy in transport and elastic properties aligned with the predominant fracture orientation. Understanding this orientation helps: (1) to avoid production interference and drainage overlap, (2) to determine the total amount of recoverable gas, and (3) to estimate the optimal number and location of infill wells (PTTC, 1999).

There have been a large number of studies on fracture characterization using anisotropy in P- and S-wave data. S-waves propagating through a fracture zone are polarized parallel and perpendicular to the fracture orientation, and can reveal different medium properties depending upon the polarization direction (e.g., Lynn et al., 1995). Another common approach is P-wave AVO analysis which reveals spatial anomalies in Poisson's ratio suggesting the presence of gas filled fractures (e.g., Lynn et al., 1995). P-to-S converted waves (Michelena et al., 1995) might be a good alternative to true shear-wave surveys because they contain nearly the same information as S-S waves but at lower experimental costs. P-to-S conversions can be generated with a traditional compressional source which makes the acquisition more effortless than true S-S wave recording, but asymmetric ray

path and the costs of recording and processing render exploration with P-S waves still more expensive than traditional P-P surveys (Perez et al., 1999).

The biggest drawback of all these methods is the ability to locate fracture zones and their orientations, but without determination of the exact location of individual fractures. These methods do not take advantage of the complex wave phenomena caused by fractures such as diffraction off fracture tips (Liu, 1997), fracture head waves (Ebrom et al., 1990), or fracture channel waves (Nihei et al., 1999). These wave phenomena are potentially more sensitive to fracture properties and geometry, and might reveal additional information such as location, orientation, fracture density and other properties.

Daley et al. (2002) performed numerical simulations of the interaction between waves and fractures. Their results observed on surface-seismic data show that the fracture-induced seismic events somewhat resemble diffraction patterns from point scatterers (Appendices A).

The objective of our investigation is the development and testing of data-processing workflows to enhance these fracture signals while suppressing reflections from approximately flat interfaces. All the workflows are based on combinations of conventional seismic data-processing tools. If the data are free of noise such as surface waves and incoherent noise, we should be left with fracture signals only after application of our workflows. These remaining fracture signals could be used for direct interpretation, imaging, or inversion.

Study Area

The study area is located in the northwestern portion of the San Juan Basin in northwestern New Mexico (Figure 1). The San Juan Basin is an important gas producing area with cumulative production by 1993 of 47.6×10^{10} m^3 from 21,000 wells (Whitehead, 1993, SJ). The San Juan Basin has an almost circular outline as indicated by the Pictured Cliffs outcrop (Figure 2). The total basin core porosity of 2.8% consists mostly of fractures and microporosity which makes this basin a perfect study area for our project. Fractures range from closed and filled to uncemented and open. Figure 2 shows the stratigraphy of the area from top to bottom, with Fruitland Coal, Pictured Cliffs Sandstone, Lewis Shale, Mesaverde group, and Mancos Shale (Whitehead, 1993). A type log is reproduced in Figure 3 presenting self potential (SP), resistivity, and conductivity of the various formations.

The Mancos formation is a thick, organic-rich, Upper Cretaceous marine shale. It is a dual-porosity, naturally fractured reservoir. Due to the tight nature of the shale matrix, reservoir development depends on extensive natural fracturing (Reeves et al., 2002). The U. S. Geological Survey estimated that 30 million bbl of recoverable resources may remain to be discovered. The matrix porosity is less than 1% and matrix permeability ranges from 0.05 to 0.1 mD (Whitehead, 1993, SJ-4). Hence, all reservoir permeability is associated with natural fractures.

The Mesaverde formation corresponds to coastal barrier sandstones deposited during a regression-transgression and alluvial cycle (Whitehead, 1993, SJ-2). The group consists of (in ascending stratigraphic order) the Point Lookout sandstone, Menefee formation, and Cliff House sandstone (Figure 2). The Point Lookout is a regressive coastal barrier

sandstone which supports most of the current production and proven reserves. The Cliff House sandstone shows small regressive pauses during the overall transgressive event. The Mesaverde coastal barrier sandstones intertongue and grade into deep-water muds of the Mancos and Lewis Shales to the northeast. The overall porosity of the formation ranges from 6% to 12%. Overall matrix permeability is less than 0.1 mD, which makes fracture characterization very important for economical gas production.

The Lewis Shale is a 350 to 500 m thick, layered reservoir composed of open marine shale and siltstone which lies between the Mesaverde formation and the Pictured Cliffs formation (Bereskin, 2002). The Lewis Shale play is a large, basin-centered, continuation type natural gas reservoir and contains estimated $271x10^{10}$ m^3 gas-in-place. Average matrix porosity and permeability are 1.72% and 0.0001 mD, which make natural fracture characterization very important for economical gas production. Two types of fractures are observed in the Lewis Shale: (1) large and discrete macro fractures, and (2) very small, hairline micro fractures within the matrix (Shirley, 2001). Both contribute to the porosity of the reservoir.

Like the Mesaverde formation, the Pictured Cliffs formation is a coastal barrier sandstone (Molennar et al., 1988), which was deposited during the final northeast regression of the late Cretaceous sea (Whitehead, 1993, SJ-2). Based on production history and permeability, the Pictured Cliffs Sandstone can be divided into three general areas. These areas are (1) the northeast: very low permeability, gas saturated, with production dependent on the fractures; (2) the central producing zone: production dependent on porosity and permeability with fracture enhancement; and (3) the southwest: the permeable and water saturated (Hoppe et al., 1992). The average core permeability of this

formation is 2.96 mD (Fasset et al., 1978), while the central producing zone has the permeability of 5-6 mD (Brown, 1978). The main reason for the low permeability toward the northeast appears to be the diagenetic change (Hoppe et al., 1992) which eventually affects the production rate.

The Fruitland formation contains up to $140x10^{10}$ m^3 of coalbed methane in place, half of which is economically recoverable. Fruitland pore systems range from overpressured to underpressured, which plays a major role in gas and water production rates and affects the carbon dioxide content in the formation (Bland et al., 1992). The Fruitland formation is Late Cretaceous in age, and 60-160 m thick. Its average thickness is 100-110 m with a general thickening trend from the southeast to the northwest (Fassett and Hinds, 1971). The Fruitland is composed of intertonguing marine and coaly nonmarine sediments consisting of sanstone, siltstone, shale and coal deposited at the edge of the Cretaceous seaway that transgressed and regressed across the basin (Whitehead, 1993, SJ-1).

2D Synthetic Seismic Section

A 2D synthetic seismic section was created to test various processing schemes to enhance the fracture signals and to suppress conventional reflections in a 2D seismic data. The subsurface model has three reflectors and thirty-four scatterers (Figure 4). The middle reflector is flat, while the top reflector is slightly dipping, and the bottom reflector is more steeply dipping. For simplicity, the fracture signals are mimicked by diffraction patterns emanating from point scatterers. The simplified model neglects conversions or

guided fracture waves, but approximates the kinematics of fracture signals observed on numerical simulations (Daley et al., 2002). The response of the scatterers was modeled using a Born integral-equation technique (Cohen et al., 1986). The data set were generated using a 50 Hz ricker wavelet with 1 ms time sampling interval. The subsurface velocity is maintained at 4000 m/s throughout the media. The data set contains 100 shots spaced at 60 m interval. Each shot was received with a split-spread array of 100 sensors with 60 m spacing. The first shot is located at 0 m with sensors between – 2970 m and 2970 m. Figure 5 presents the stacking chart of the data. Figure 6 shows the seismogram from the shot located at 840 m. This seismogram with three reflections and numerous fracture signals will serve as a benchmark to evaluate the effectiveness of our data-processing workflows.

Processing Schemes-> Data-Processing Workflows

We developed and tested seven data processing flows to enhance the fracture signals and to suppress the reflection hyperbolas from the synthetic seismic section.

Diode Filter:

(1) Each shot gather is split into positive and negative offsets.

(2) In each half gather, backscattered energy propagating toward the source is removed by dip filtering in the F-K domain, while forward scattered energy propagating away from the source is kept in place (Figure 7). The data is sorted into receiver gathers, and the procedure is repeated.

(3) This process removes backscattered energy, but leaves the traditional reflection hyperbolas (Figure 8(A)). Hence, the reflection section is subtracted from the original section to generate the fracture-signal section.

As can be seen in Figure 8(B), all three reflection hyperbolas have weakened. However, parts of the fracture signals have been removed too.

Figure 8(A) illustrates that parts of the fracture signals cannot be removed in step 2 because they propagate away from the source. Hence, these unsuppressed parts of the fracture signals are being removed in step 3.

The data could be spatially aliased at large offsets, and hence, dip filtering might produce undesired artifacts. Trace interpolation might be required to overcome the spatial aliasing. In this particular case, two traces were interpolated between each geophone interval to avoid spatial aliasing while applying dip filter.

Dip-Filtering in Common-Offset Gather:

(1) The data are sorted into the common-offset domain. True reflections are mapped to nearly linear events, but fracture signals are deformed strongly. Figures 9(A) and 9(B) show offset gathers at offsets –30 m (near-offset) and –2970 m (far-offset). Fracture signals on near offset gathers have conical shapes, while they become flat topped at the far offset (Claerbout, 1985). This shows that fracture signals at the far offset will be attenuated when dip filters are applied to remove the flat events.

(2) A dip filter in the F-K domain with dip –0.15 ms/km to 0.15 ms/km is applied to remove flat or near-flat events and the data is sorted back into shot gather.

This method is producing good results. The middle reflector is completely removed, the top reflector is suppressed substantially, and the bottom reflector has been weakened (Figure 9(C)). Some fracture signals are partially suppressed too, because their flat tops on far-offset gathers (Figure 9(B)) are removed by the dip filter.

NMO – Dip Filter:

(1) Shot gathers are normal-moveout (NMO) corrected with the appropriate stacking velocity.

(2) After NMO correction, the reflections are approximately flat, while the fracture signals are strongly deformed. The flat events are removed by dip filtering in F-K domain for dips between –0.15 ms/km to 0.15 ms/km, and the remaining section is transformed back by inverse NMO. The resulting gather is shown in Figure 10.

The result is satisfactory. The middle reflector is completely suppressed, but the bottom and top reflectors could not be removed completely due to their dip.

NMO–DMO-Dip Filter:

A potential fix for dipping reflectors is application of a dip-moveout correction (DMO). DMO increases the differential moveout between diffractions and reflections (Kent et al., 1996), and can be applied to distinguish reflections from fracture signals. We applied the following processing flow:

(1) Apply NMO correction.

(2) The data are sorted into common-offset gathers and DMO is applied. The data are sorted back into shot gather.

(3) All flat events are removed for dips between –0.15 ms/km to 0.15 ms/km.

(3) Apply inverse NMO (Figure 11).

The results were nearly indistinguishable from the NMO-dip filter shown in Figure 10. DMO did not affect the reflections noticeably, but introduced artifacts. Hence, DMO was not applied in any of the following flows either.

Eigenvector Filter:

The Eigenvector filter is similar to K-L transform (Hsu, 1990). A 2D NMO-corrected seismic section is treated as a 2D matrix, which can be decomposed into its eigensections with their associated eigenvalues. Large eigenvalues represent flat-reflection events, while small eigenvalues represent random noise and less prominent events. If S (t, x) is our data matrix, its corresponding singular value decomposition can be written as $S=U\Sigma V^T$, where U and V are unitary matrixes containing the left and right eigenvectors of S, and Σ is a diagonal matrix carrying the eigenvalues of S (Bihan et al., 2001).

In NMO-corrected shot gather, flat reflectors can be removed by discarding eigensections. We suppressed the reflections by discarding eigensections with eigenvalues above the 80^{th} percentile.

The method produced a very good result for the middle and top reflectors which are almost horizontal (Figure 12). The steeply dipping bottom reflector is suppressed, although noise artifacts were introduced. Fracture signals, however, are completely intact.

Harlan's Signal/Noise Separation Technique:

Harlan et al. (1984) presented a signal-noise separation scheme to separate events that can be focused by a linear transformation (signal) from events that cannot be focused (noise). NMO correction is applied on the data so that the reflections become linear while the fracture signals are strongly deformed. Harlan's method is applied to discriminate all the linear events in the data while the rest of the events are treated as noise. To apply this scheme, data were sorted into the absolute offset domain. Using a reference offset of 2,000 m, signal and noise sections were generated containing the linear events (reflections) and fracture signals, respectively. Inverse NMO was applied on the noise section to obtain the fracture signals (Figure 13).

The method produced good results with some added artifacts. Middle and top reflections are completely removed, while parts of the bottom reflector remained due to steep dip.

Radon Filtering:

Hampson (1986) proposed multiple suppression using generalized Radon filtering. After Radon transform of a NMO-corrected data along planar integration paths, diffractions, scattering, conversions, and other non-reflection events have non-zero residual moveout in Radon space, while the reflections should have zero residual moveout. Hence, reflections can be removed by suppressing events with zero residual moveout in Radon space. The workflow consists of the following steps:

1) NMO correct the data to flatten reflections.
2) Convert the data to Radon space which maps reflectors to zero residual moveout.

3) Define and apply a filter in the Radon domain which suppresses the events with zero and near-zero residual moveout.
4) Convert the data back into the time-space domain.
5) Inverse NMO was applied.

Middle and top reflectors are subdued (Figure 14) while fracture signals persist, but the procedure also introduced some artifacts. The bottom reflector remains due to its steep dip. This method is computationally very slow compared to other methods because the Radon transformations are very time consuming. The success of this method depends on the difference in residual moveout between the reflections and fracture signals.

3D Real Data Set from San Juan Basin

ConocoPhilips provided an NMO corrected 3D data set from the San Juan Basin (Freeman, 1999). The receivers are arranged in a brick pattern, while shots were placed along roads (Figure 15).

The 3D data were sorted by shot, inline receiver numbers, and crossline receiver numbers to inspect the shot gathers as illustrated in Figure 16. This particular shot gather shows three receiver crosslines. Figure 17 shows all the traces from receiver crossline (3), sorted by their receiver inline numbers. We notice undulating events, which we suspect to be fracture signals.

Due to the irregular geometry of the survey and lacking 3D implementations of some filters, we only used three filters to detect and enhance these fracture signals:

Dip-Filter: The data were already NMO corrected. Reflections are approximately flat, while scattering and fracture signals are deformed in bizarre manners. A fan shaped dip-filter in F-K domain was applied to remove the flat reflectors. Figure 18 shows the data from receiver crossline (3) after application of the dip-filter. The reflections are mostly suppressed, while fracture signals were barely perturbed or removed.

Eigenvector Filter: This filter is similar to the one used for the 2D synthetic data set. Figure 19 shows the receiver crossline (3) after applying the Eigenvector filter to remove the top 10% of the eigenvalues. Reflectors are largely suppressed and fracture signals are almost intact. This method is computationally slow compared to the F-K dip filtering.

Radon Filter: The filter is the same as for the 2D case. Figure 20 shows the result after application of the Radon filter to crossline (3). The method does not produce satisfactory results due to the low residual moveout difference between reflectors and fracture signals.

Discussion and Conclusion

We tested several workflows to enhance fracture signals, and found that every scheme has its advantages and limitations. NMO-dip filtering to remove flattened reflection events is computationally very fast and produces good results, but for dipping reflectors, it may partially leave reflections in the resultant section. If we examine Figure 10, we observe that only the middle reflector is completely removed, while parts of the bottom and the top reflectors are still present because of their dips. The diode filter completely removes the reflections (Figure 8), but also affects the fracture signals. Dip-filtering in the common-offset gather produces good results. Reflections are almost removed except

the bottom reflector (Figure 9(c)). Its independence on the NMO velocity makes Diode filter and common-offset dip filter easy to apply on a 2D data with uncertain NMO velocities. Both the filters are computationally very efficient. They require, however, high folds in receiver and angle-dependent offset gathers which may not be available for irregular 3D survey. Application of DMO to improve removal of dipping reflectors was unsuccessful and introduced incoherent noise artifacts (Figure 11). The Eigenvector filter was applied very efficiently both for 2D and 3D data sets. This method added some noise to the data, but produced good results. The fracture signals were well preserved both in 2D and 3D data (Figures 12 and 19). For large data sets, however, Singular Value Decomposition (SVD) could be computationally expensive. Harlan's method (Figure 13) is producing good results with some added artifacts. This method is slow compared to other methods because the Tau-P transformations need to be applied to focus the linear events. Due to the lack of a 3D implementation, we were unable to test Harlan's method (1984) on 3D data. Radon filtering was applied on 2D and 3D datasets which removed horizontal or near-horizontal reflections from the data (Figures 14 and 20). Choice of parameters is crucial for a successful application of this method. Moreover, this filter could be computationally very expensive for large datasets.

Prestack migration might be another approach to focus the fracture signals, but it was not applied on these data because of time constraints and the realization that some fracture signals may correspond to P-S conversions. Furthermore, prestack migration would greatly benefit from enhanced fracture signals and suppressed reflections.

We have not proven that our "fracture signals" are truly emanating from discrete fractures. They could also be caused by cavities, pinnacles or other point scatterers, or

lothologic heterogeneity. The Mesaverde formation in the San Juan Basin is highly fractured on all scales. It is quite possible that some of our “fracture signals” were really caused by fractures. At worst, we identified seismic events which should be investigated further and whose origin should be located. Potential methods to resolve the nature of our “fracture signals” include numerical forward modeling, multicomponent high-resolution surface seismic experiments, multicomponent VSP experiments, or even single-well imaging.

References

Bereskin, S. R., 2002, Geologic and production characteristics of the Lewis Shale (San Juan Basin, New Mexico) as results apply to other Cretaceous “shales” of the Western Interior; the next unconventional reservoir of the Rocky Mountains, USA and Canada: Reservoir, 29, no. 6.

Bihan, N. L., Lariani, S., and Mars, J., 2001, Seismic cube decomposition before reservoir characterization: 71st Ann. Internat. Mtg., Soc. Expl. Geophys., Expanded Abstract, 1564-1567.

Bland, D. M., 1992, Colabed Methane from the Fruitland Formation, San Juan Basin, New Mexico: New Mexico Geological Society Guidebook, 43rd Field Conference.

Brown, C. F., 1978, Fulcher Kutz Pictured Cliffs; in Fasset, J. E., ed., Oil and Gas Fields of the Four Corners Area: Four Corners Geological Society, p. 307.

Claerbout, J.,1985, Imaging the Earth’s Interior, 163-165.

Coates, R. T., and Schoenberg, M., 1995, Finite-difference modeling of faults and fractures: Geophysics, **60**, no. 5, 1514-1526.

Cohen, J. K., Hagin, F. G., and Bleistein, N., 1986, Three-dimensional Born inversion with an arbitrary reference: Geophysics, **51**, no. 8, 1552-1558.

Daley, T. M., Nihei, K. T., Myer, L. R., Majer, E. L., Queen, J. H., Fortuna, and M., Murphy, J., 2002, Numerical modeling of scattering from discrete fracture zones in a San Juan Basin gas reservoir: 72nd Ann. Internat. Mtg., Soc. Expl. Geophys., Expanded Abstract, 109-112.

Durrast, H., Rasolofosaon, P. N. J., and Siegesmund, S., 2002, P-wave velocity and permeability distribution of sandstones from a fractured tight gas reservoir: Geophysics, **67**, no. 1, 241-253.

Ebrom, D. A., Tatham, R. H., Sekharan, K. K., McDonald, J. A., and Gardner, G. H. F., 1990, Hyperbolic traveltime analysis of first arrivals in an azimuthally anisotropic medium: A physical modeling study: Geophysics, **55**, no. 2, 185-191.

Fassett, J. E., Arnold, E. C., Hill, J. M., Hatton, K. S., Martinz, L. B. and Donaldson, D. A., 1978, Stratigraphy and oil and gas production of northwest New Mexico; in Fassett, J. E., ed., Oil and Gas Fields of the Four Corners Area; Four Corners Geological Society, p. 46-61.

Fassett, J. E., and Hinds, J. S., 1971, Geology and fuel resources of the Fruitland Formation: U. S. Geological Survey, Professional Paper 676, 76 p.

Freeman, D., 1999, No Seismic 'Footprints' left Behind: AAPG Explorer, October, 10.

Grechka, V., and Tsvankin, I., 1998, 3-D description of normal moveout in anisotropic inhomogeneous media: Geophysics, **63**, no. 3, 1079-1092.

Hampson, D., 1986, Inverse velocity stacking for multiple elimination: 56th Ann. Internat. Mtg., Soc. Expl. Geophys., Expanded Abstract, 422-424.

Harlan, S., Claerbout, J., and Roca, F., 1984, Signal/noise separation and velocity estimation: Geophysics, **53**, no. 11, 1869-1880.

Hoppe, W. F., 1992, Hydrocarbon Potential and Stratigraphy of the Pictured Cliffs, Fruitland and Ojo Alamo Formations in the Northeastern San Juan Basin, New Mexico: New Mexico Geological Society Guidebook, 43rd field conference.

Hsu, K., 1990, Wave separation of feature extraction of acoustic well-logging waveforms using Karhunen-Loeve transformation: Geophysics, **55**, no. 2, 176-184.

Kent, G. M., Kim, I. I., Harding, A. J., Detrick, R. S., and Orcutt, J. A., 1996, Suppression of sea-floor-scattered energy using a dip-moveout approach – application to the mid-ocean ridge environment: Geophysics, **61**, no. 3, 821-834.

Liu, E., 1997, Diffraction of seismic waves by cracks with application to hydraulic fracturing: Geophysics, **62**, no. 1, 253-265.

Lynn, H. B., Simon, K. M., Layman, M., Schneider, R., Bates, C. R., and Jones, M., 1995, Use of anisotropy in P-wave and S-wave data for fracture characterization in a naturally fractured gas reservoir: The Leading Edge, **14**, 887-893.

Michelena, R. J., Ata, E., and Sierra, J., 1994, Exploiting P-S converted waves: part I, Modeling the effects of anisotropy and heterogenities: 64th Ann. Internat. Mtg., Soc. Expl. Geophys., Expanded Abstract, 236-239.

Nihei, K. T., Weidong, Y., Myer, L. R., Cook, N. G. W., and Schoenberg, M., 1999, Fracture channel waves: Journal of Geophysical Research, **104**, no. B3, 4769-4781.

Perez, M. A., Grechka, V., and Michelena, R., 1999, Fracture detection in a carbonate reservoir using a variety of seismic methods: Geophysics, **64**, no. 4, 1266-1276.

PTTC, 1999: http://www.pttc.org/solutions/416.pdf

Reeves, S., Billingsley, R., Embry, G., and Lindsey, R., 2002, Mancos shale oil potential large on Jicarilla lands in New Mexico: Oil and Gas Journal, 100, no. 49, 42-50.

Sheriff, R. E., Geldart L. P., 1995, Exploration Seismology 2nd Edition, 159-163.

Shirley, K., 2001, Lewis not overlooked anymore: AAPG Explorer, March 2001.

Whitehead, III, N. H., 1993, San Juan Basin, in Atlas of Major Rocky Mountation Gas Reservoirs, Robertson, J. M., Broadhead, R. F., Gorody, A. W., and Hjellming, C. A. (Eds), Gas Research Institute, 118-132.

Figures

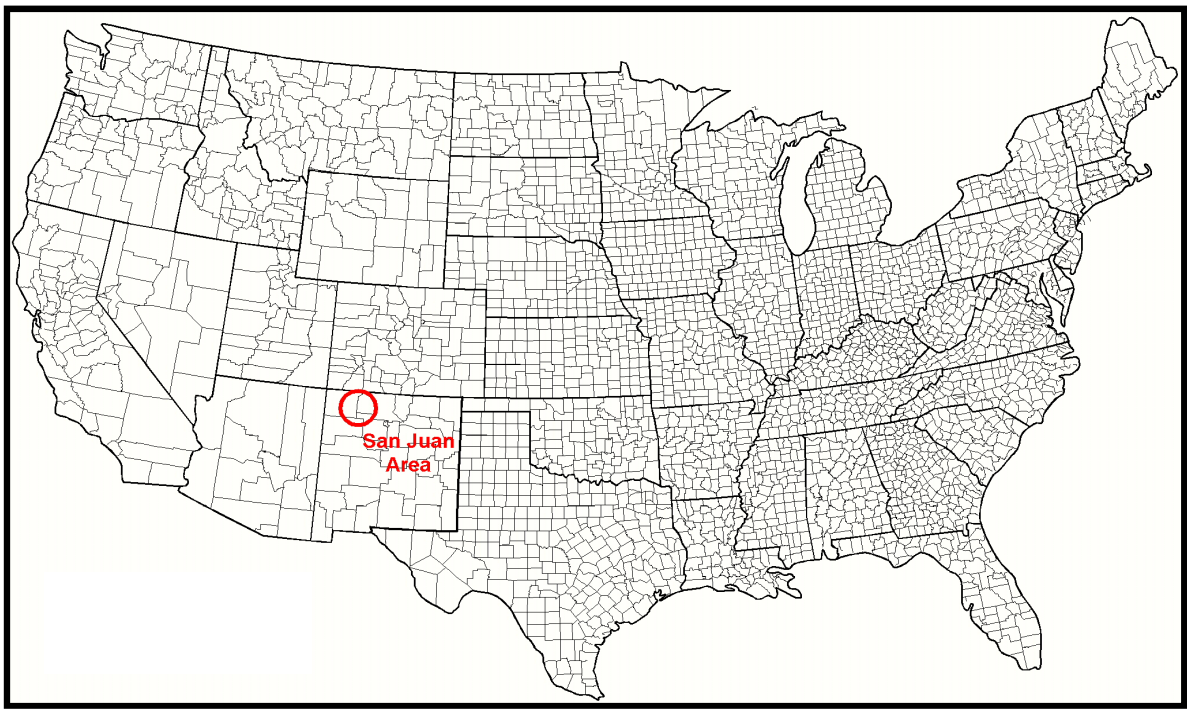

Figure 1: Location Map
Location map showing the San Juan Basin as the shaded area. The basin covers 17,350 square cubic km and is the second largest natural gas reservoir in the United States.

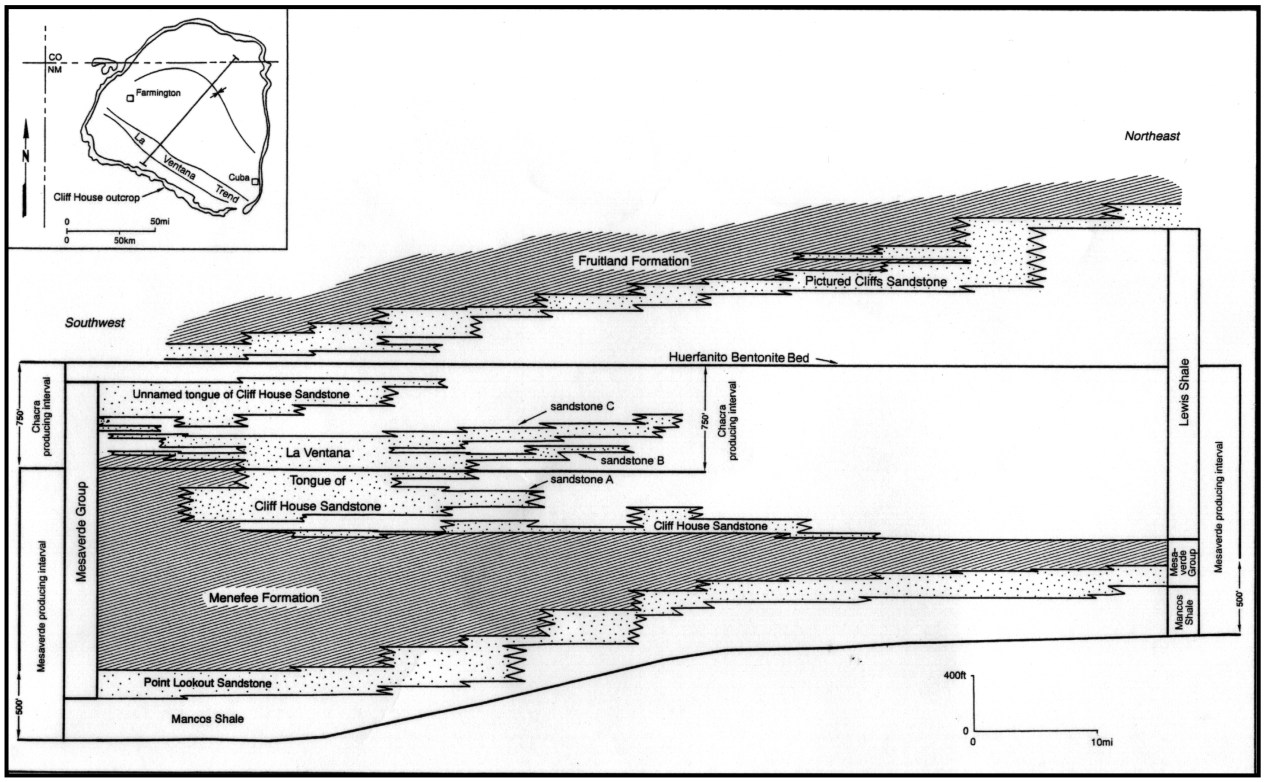

Figure 2: Stratigaphy of the San Juan Basin (Whitehead, 1993, SJ-3)
The San Juan Basin is defined by the Pictured Cliff outcrops and is almost circular as shown in the top left corner. Mesaverde group, which is the most dominating horizon in the area, is mainly characterized by Point Lookout Sandstone, Menefee coal formation and Cliff House Sandstone. Notice that the Cliff House Sandstone shows regressive pauses during overall transgressive events. The Fruitland and Menefee are two major coal bed horizons. The Lewis Shale lies above Mesavede and below Pictured Cliff formations.

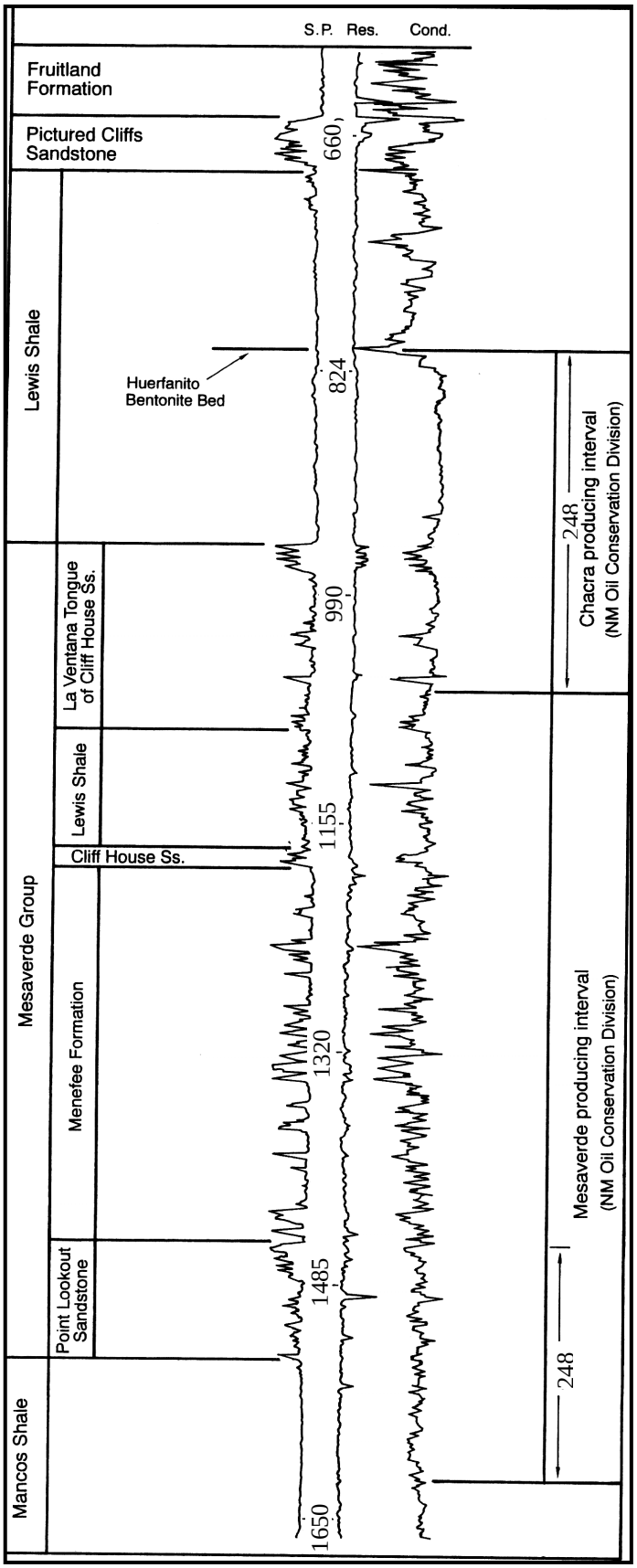

Figure 3: Type well log from the San Juan Basin (Whitehead, 1993, SJ-3)

The Mesaverde Group is the main producing and thickest interval of the basin. The Coastal barrier sandstones of the Mesaverde Group intertongue into the Lewis Shale. Depths of the horizons are in meters.

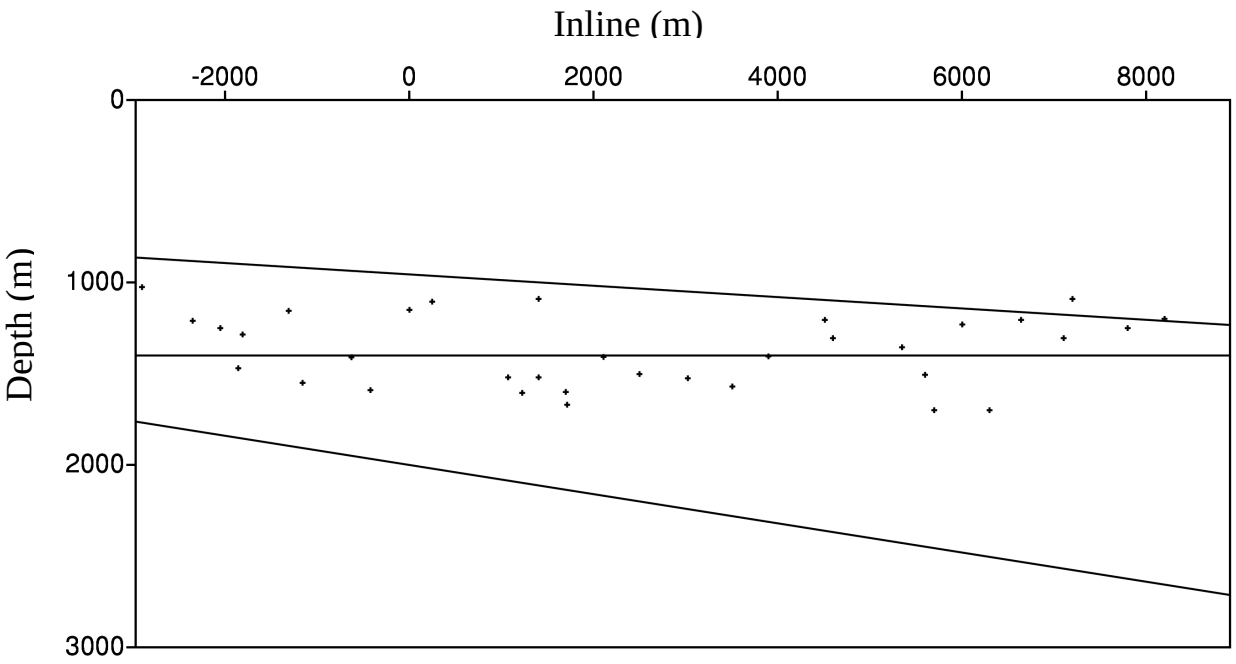

Figure 4: Subsurface model used to generate 2D synthetic data
There are 3 reflectors and 34 scatterers in the subsurface model. Middle reflector is flat while top reflector is slightly dipping and bottom reflector is steeply dipping. Subsurface velocity is maintained at 4000m/s.

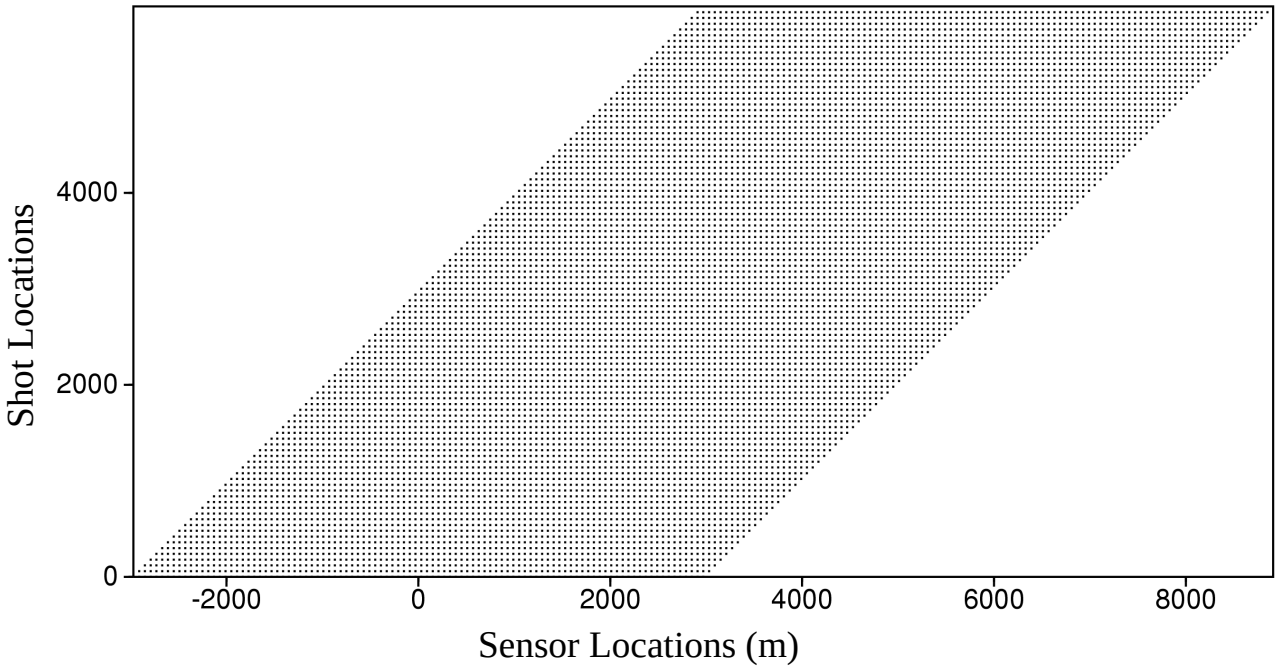

Figure 5: Stacking chart of synthetic data
The data set contains 100 shots at 60m intervals. The first shot is located at 0m. One hundred sensors record each shot at 60m interval with split spread geometry.

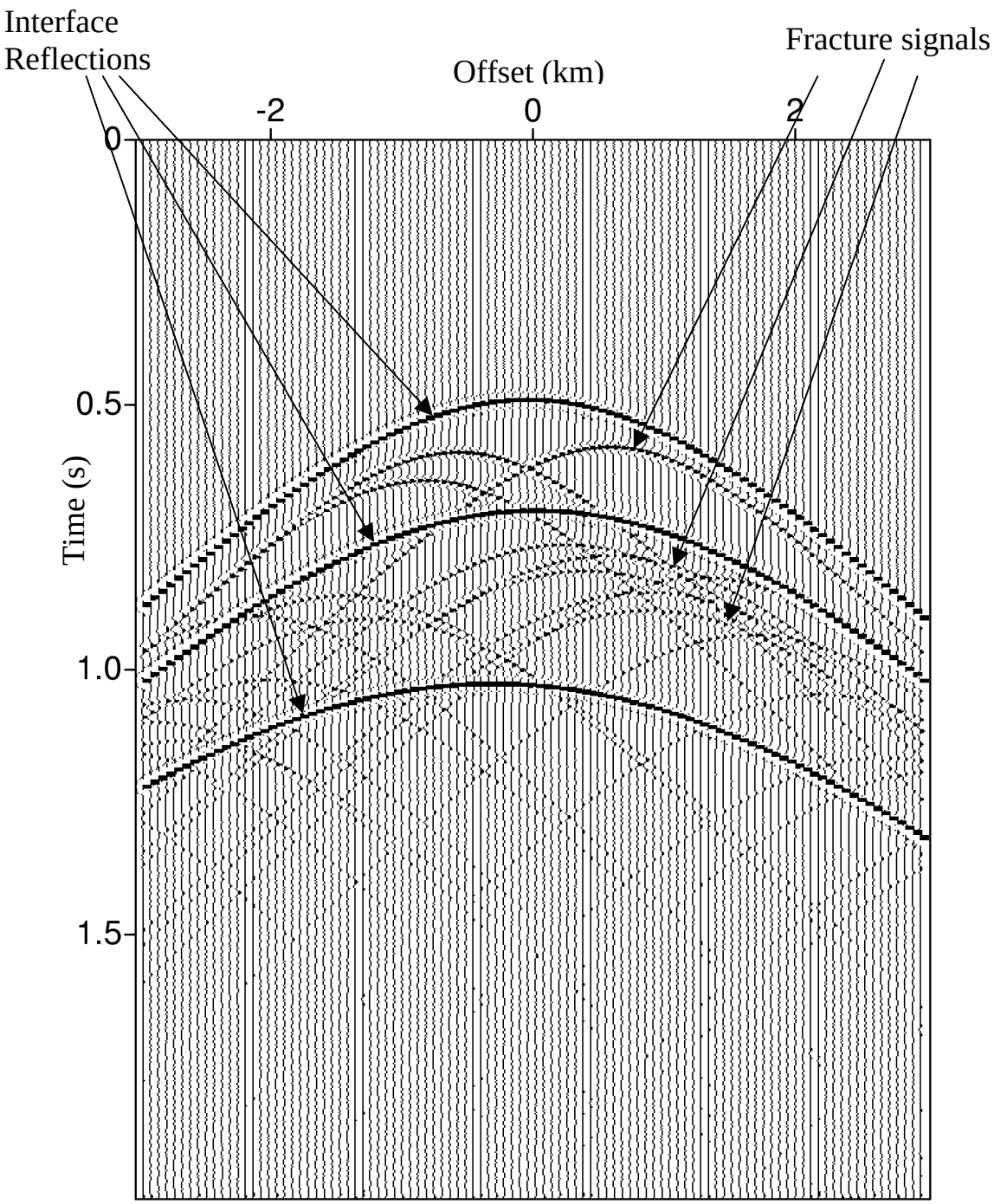

Figure 6: Shot gather at 840 m.
Three reflection hyperbolas originate from three reflectors in the subsurface. The other events are diffraction hyperbolas from point scatterers which we call fracture signals because they mimick the kinematics of fracture events observed by Daley et al., 2002.

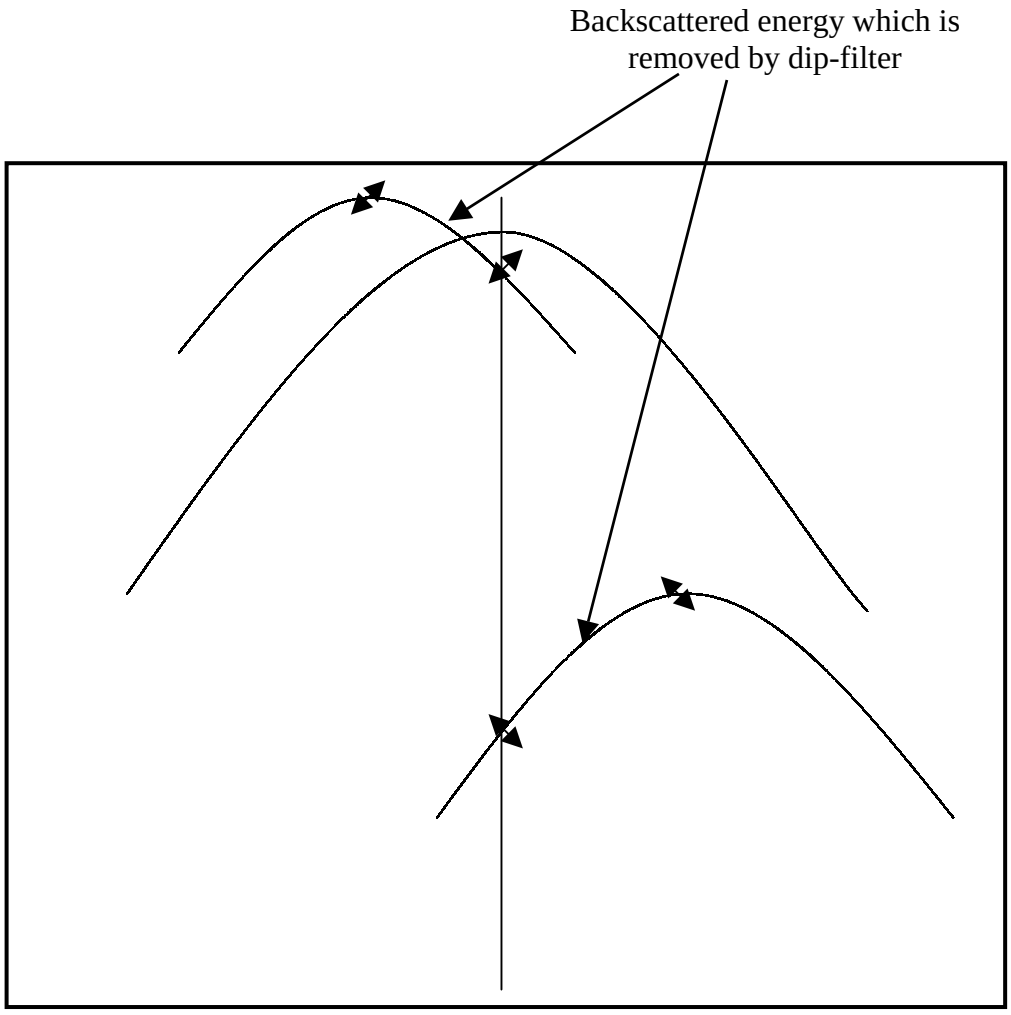

Figure 7: Backscattered energy which is dip-filtered.
The figure shows one reflection hyperbola and two diffraction patterns in a shot gather. The vertical line divides positive and negative offsets. Events bounded by the little arrows correspond to backscattered energy which are removed by dip filtering.

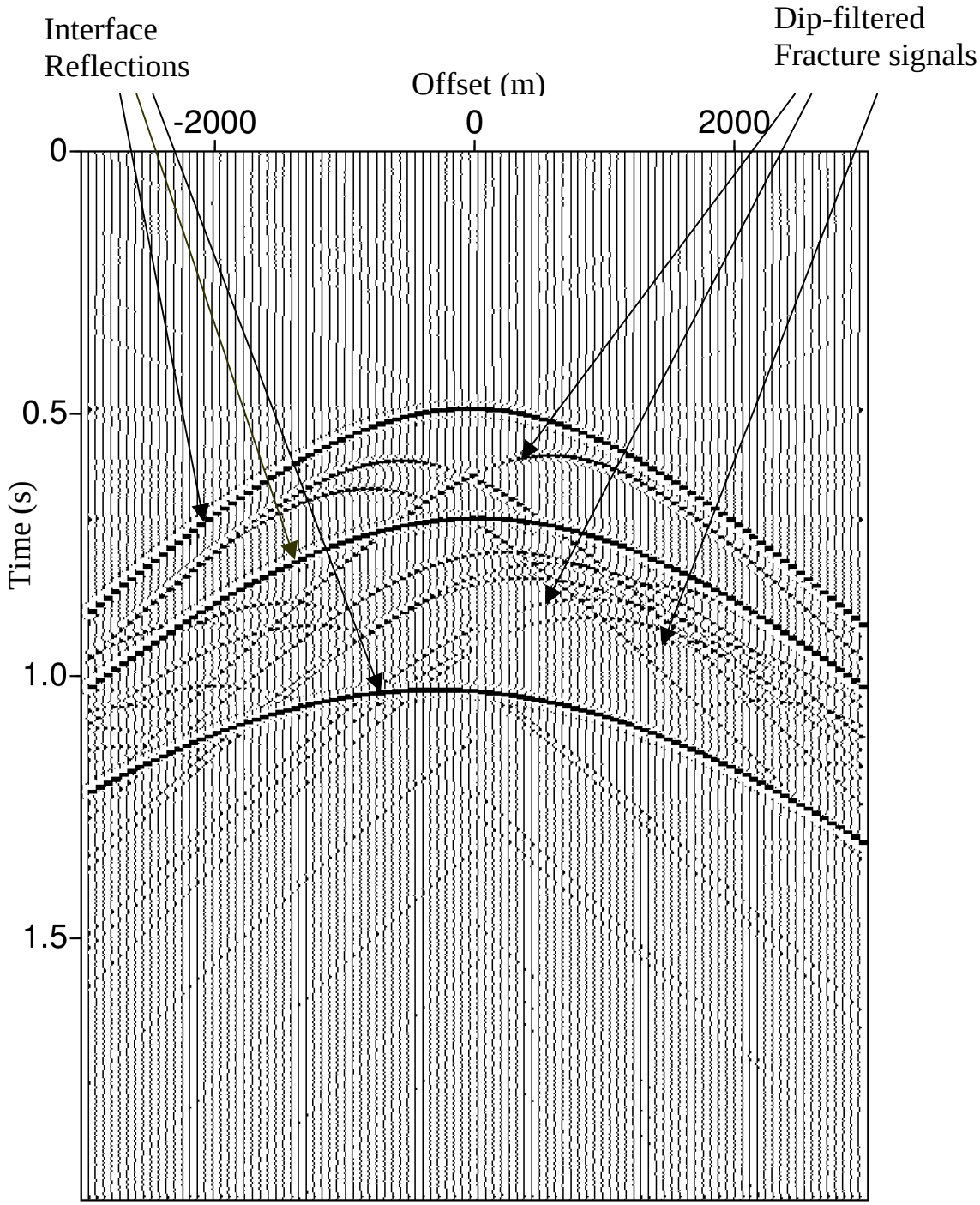

Figure 8(A): Shot gather after dip filtering backscattered energy. Reflection hyperbolas are almost intact. Backscattered energy of fracture signals are suppressed.

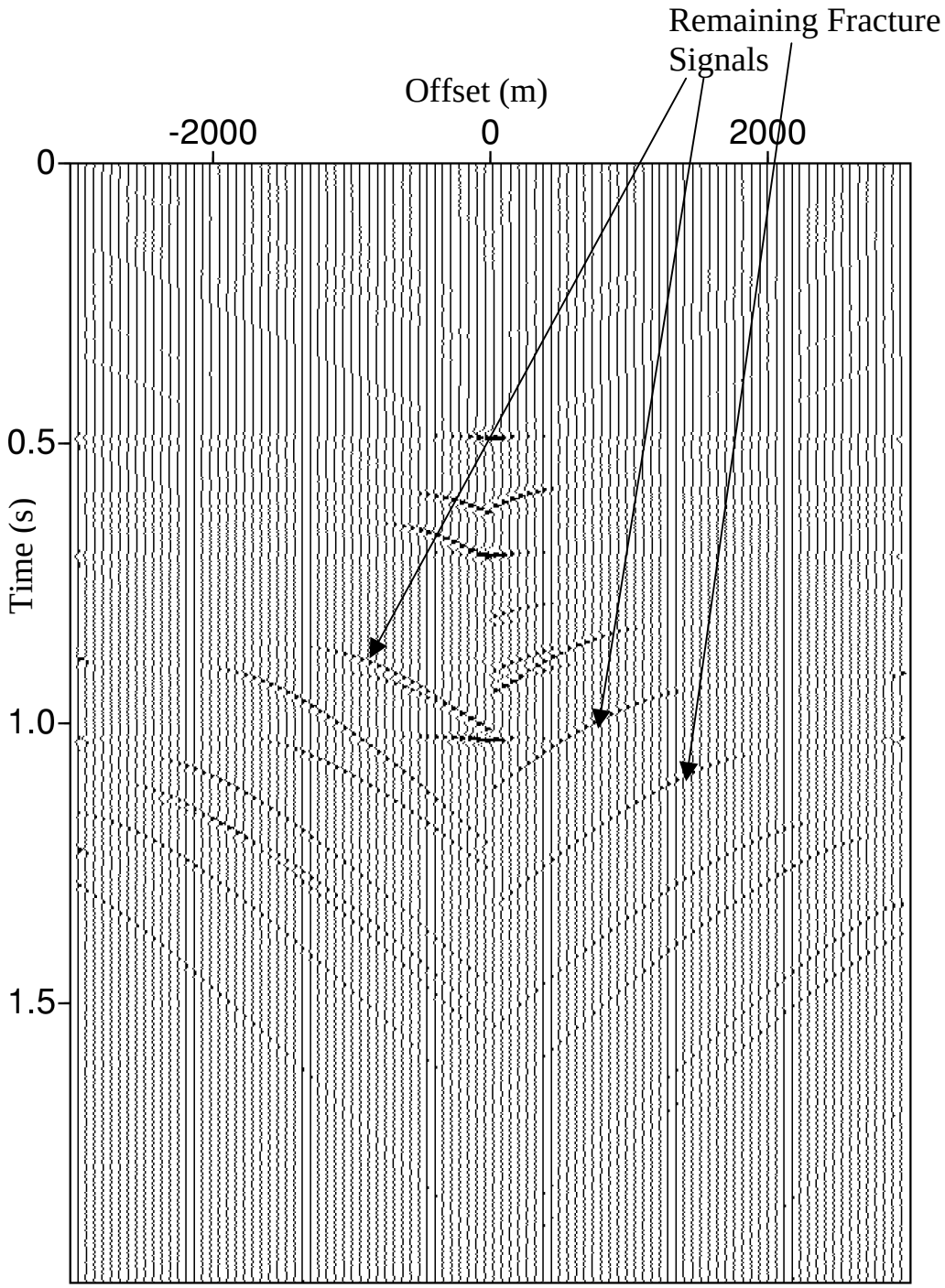

Figure 8(B): Shot gather after diode filtering.
Above figure was generated by subtracting Figure 8(A) from original section (Figure 6). Reflections are eliminated completely. Other half of the fracture signals are suppressed too due to dip filtering.

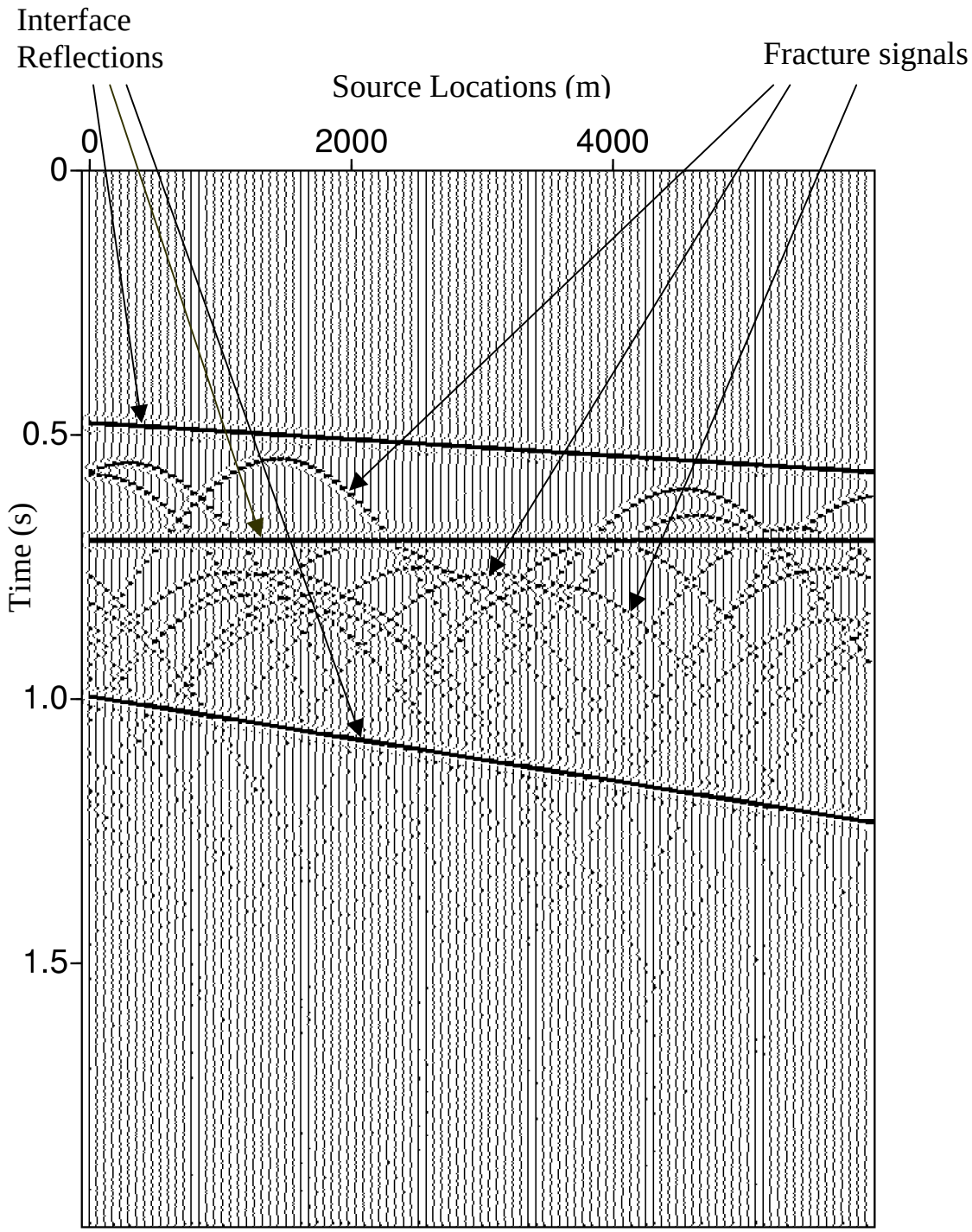

Figure 9(A): Common-offset gather at offset – 30 m.
Reflections are linear events while fracture signals are deformed.

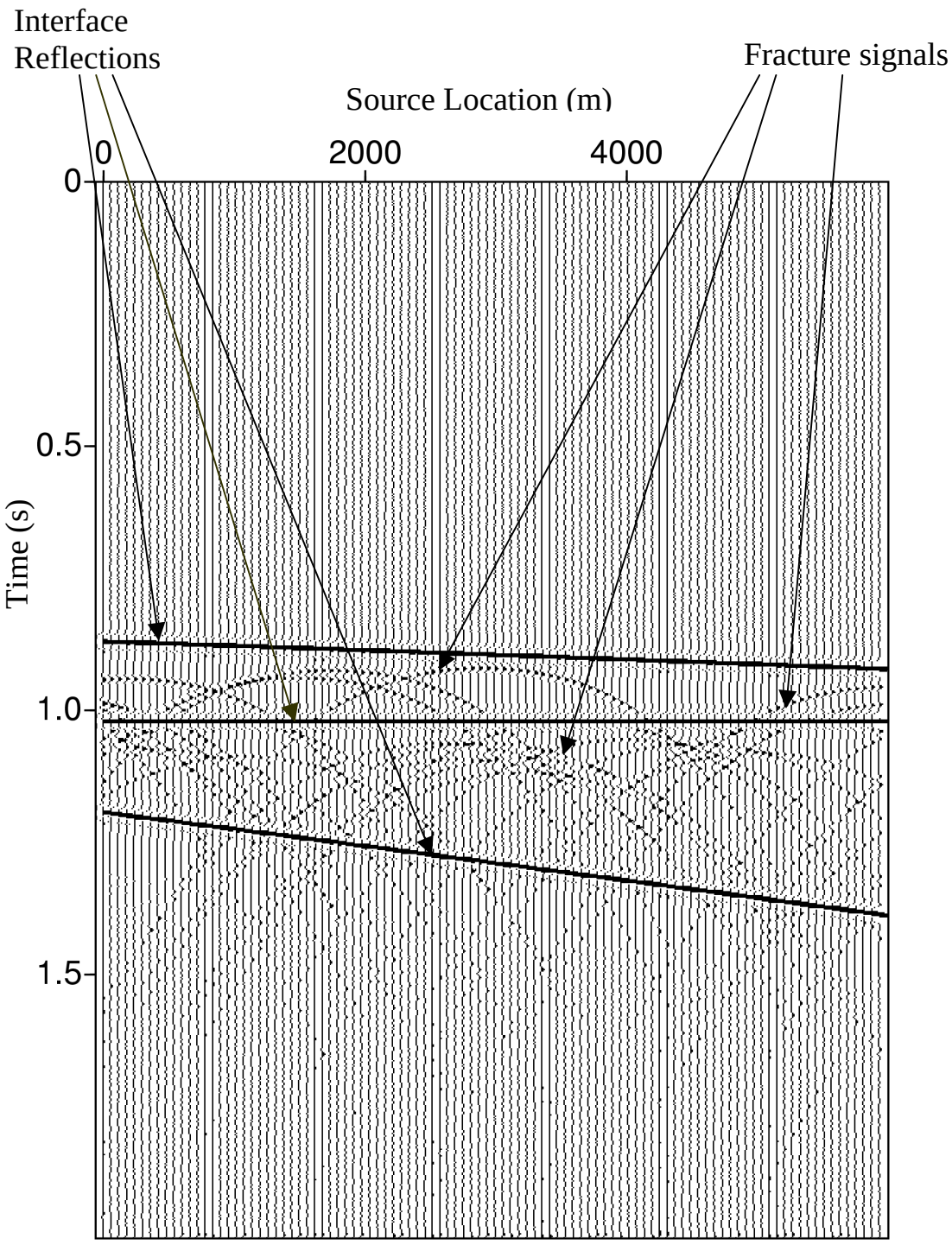

Figure 9(B): Common-offset gather at offset – 2970 m.
Reflections are flat events while fracture signals are deformed. Note that top of the fracture signals is also flattened and will be removed by dip filtering of flat linear events.

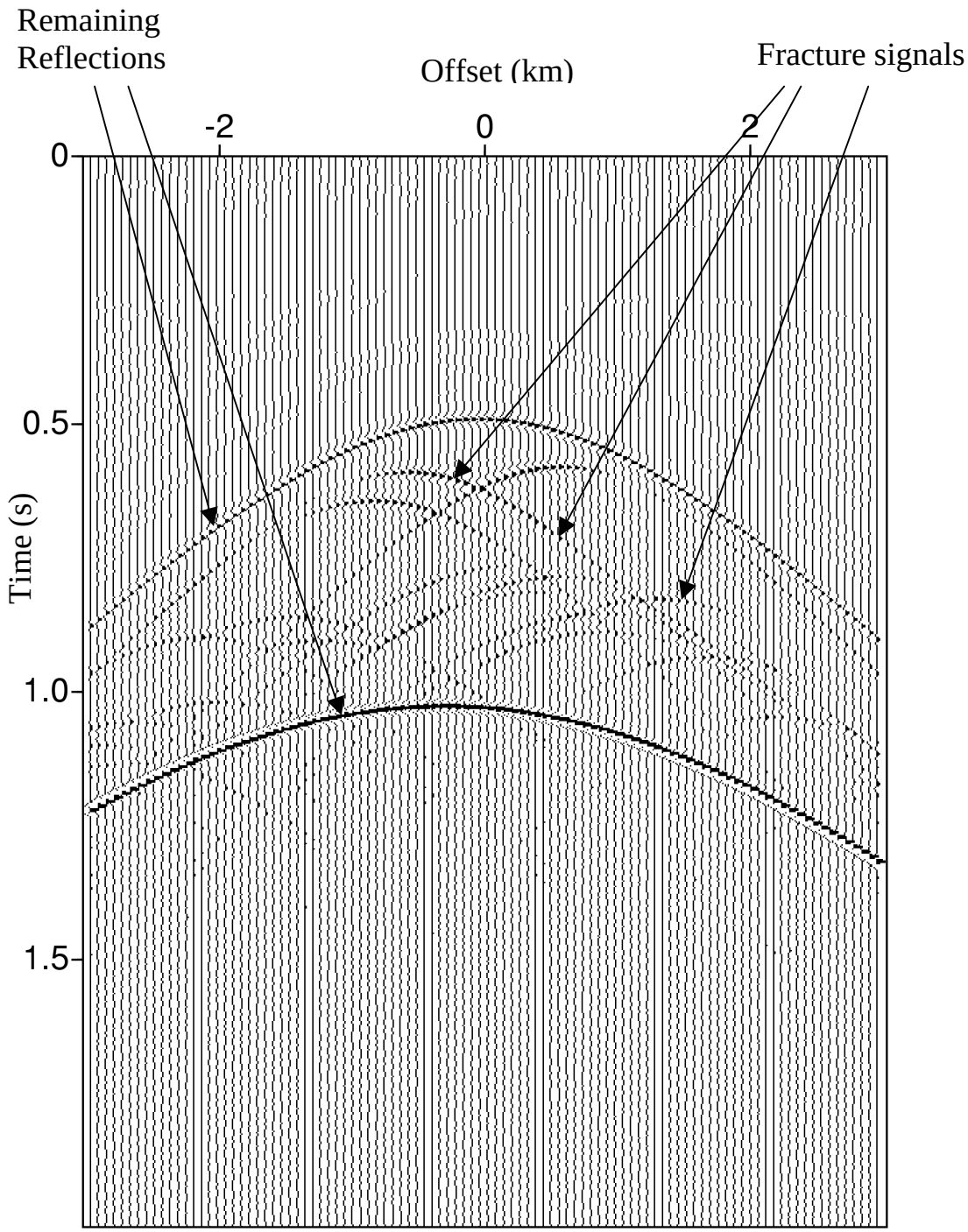

Figure 9 (C): Shot gather after applying dip filter on common-offset gather. Middle reflector is completely removed; the top and bottom reflectors were not suppressed completely because the dip filter was applied conservatively to remove only flat or near-flat events. Fracture signals are suppressed partially because they are flattened on common-offset gathers at large offsets.

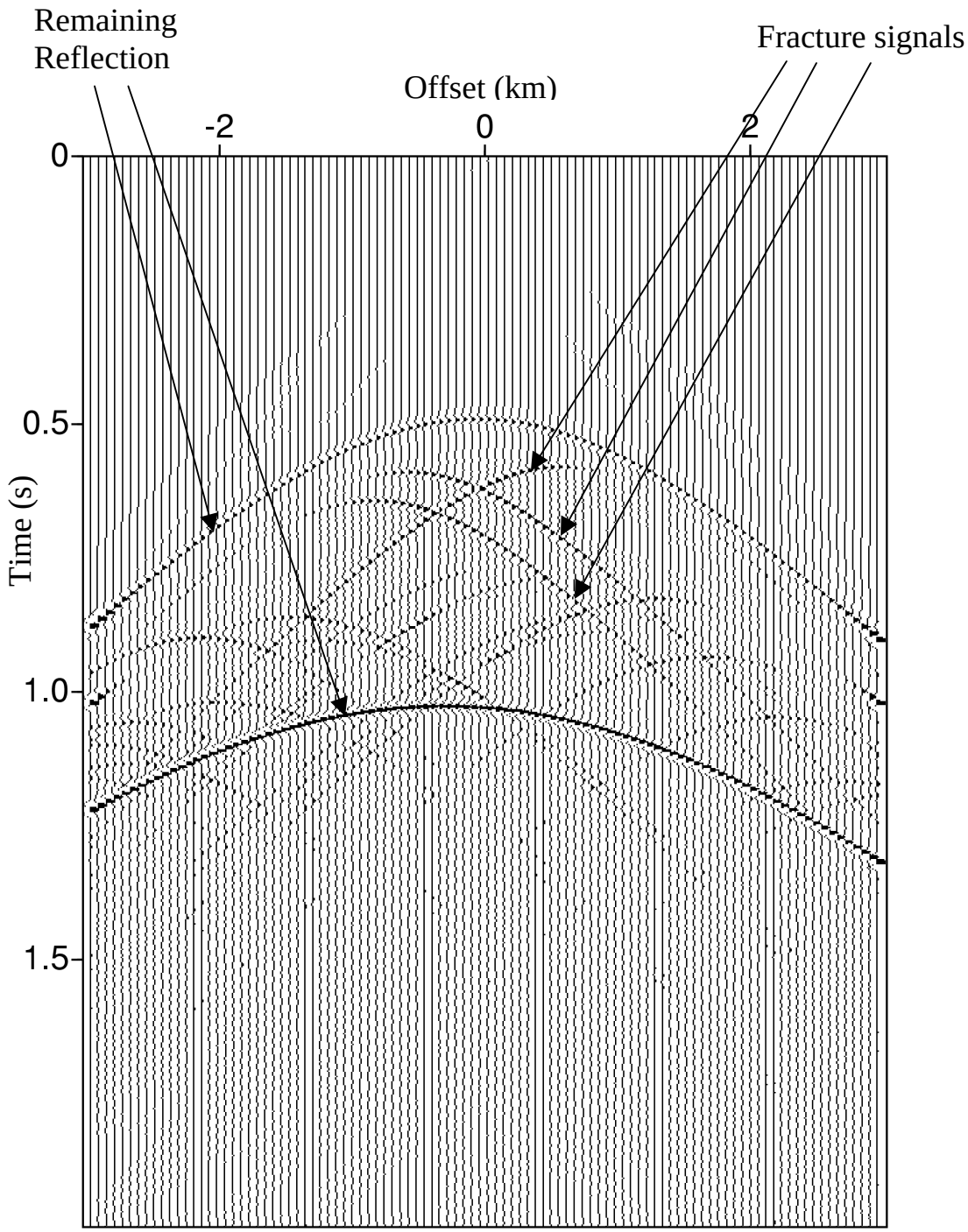

Figure 10: Shot gather after applying NMO-dip filter.
The bottom reflector is not completely removed because of its steep dip. The diffraction patterns are affected too.

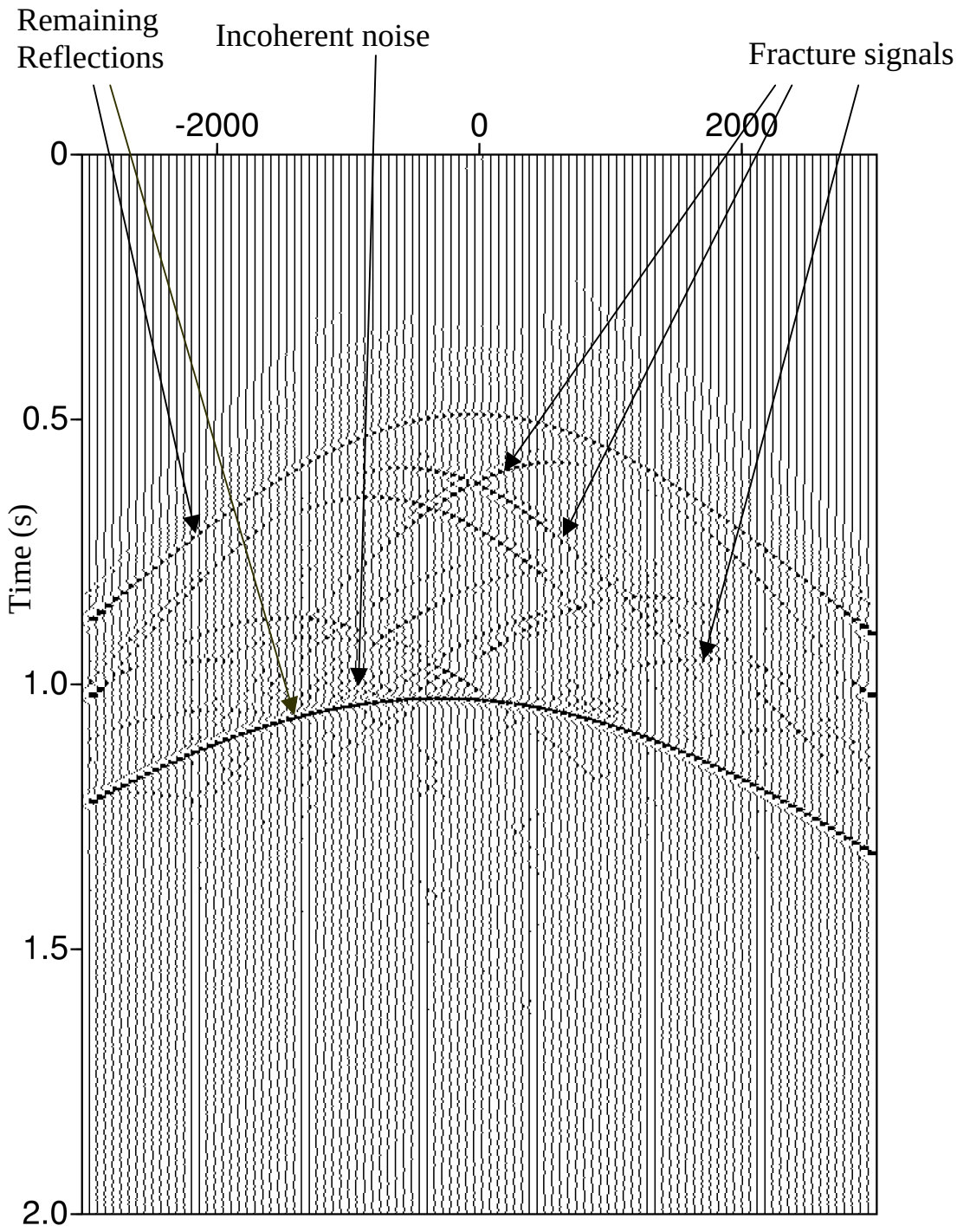

Figure 11: Shot gather after applying NMO-DMO-Dip filter.
The Middle and top reflectors are almost removed. Incoherent noise is introduced to the data by the DMO.

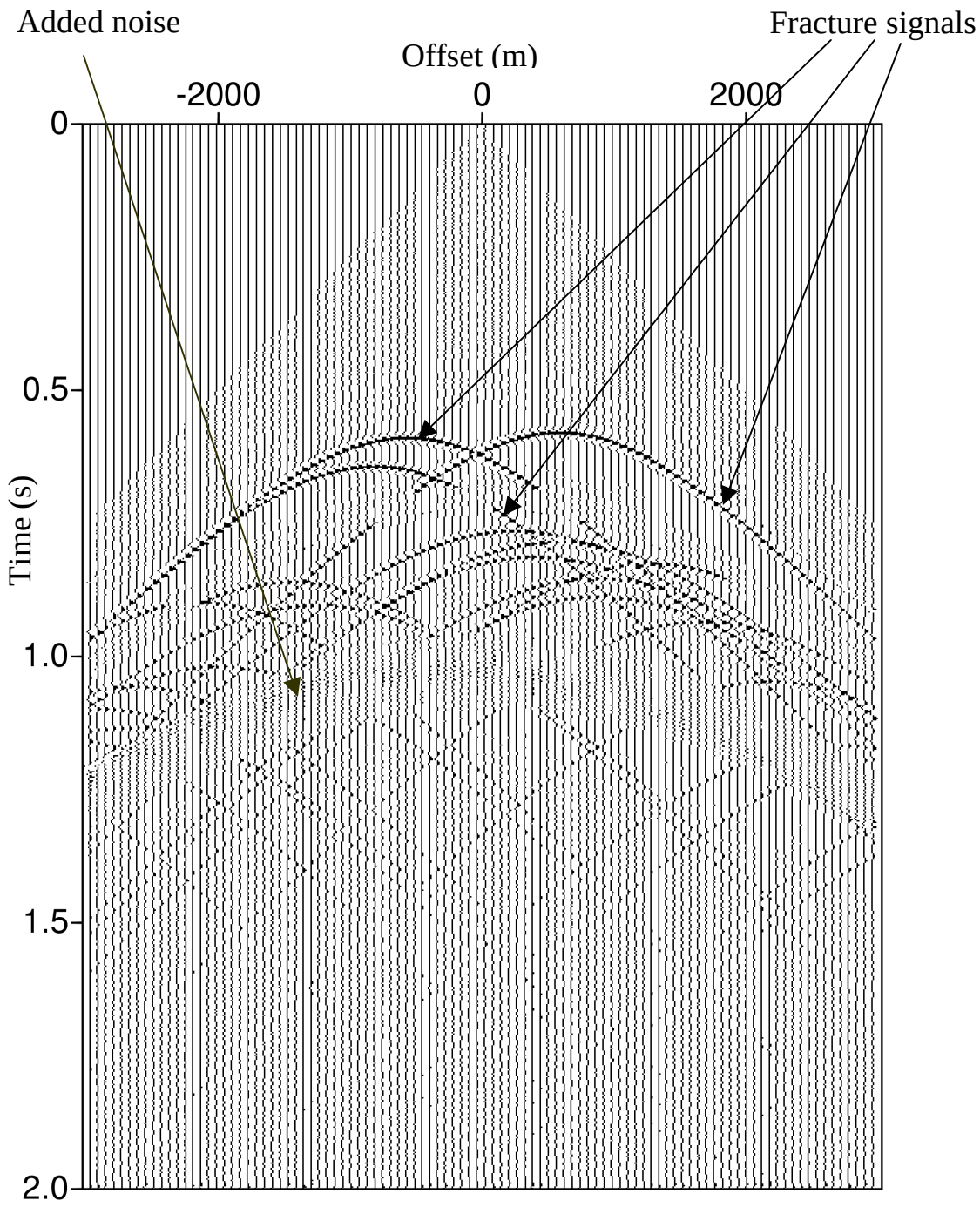

Figure 12: Resultant data after applying Eigenvector Filter.
Above section was generated after setting top 20% eigenvalues as zero.

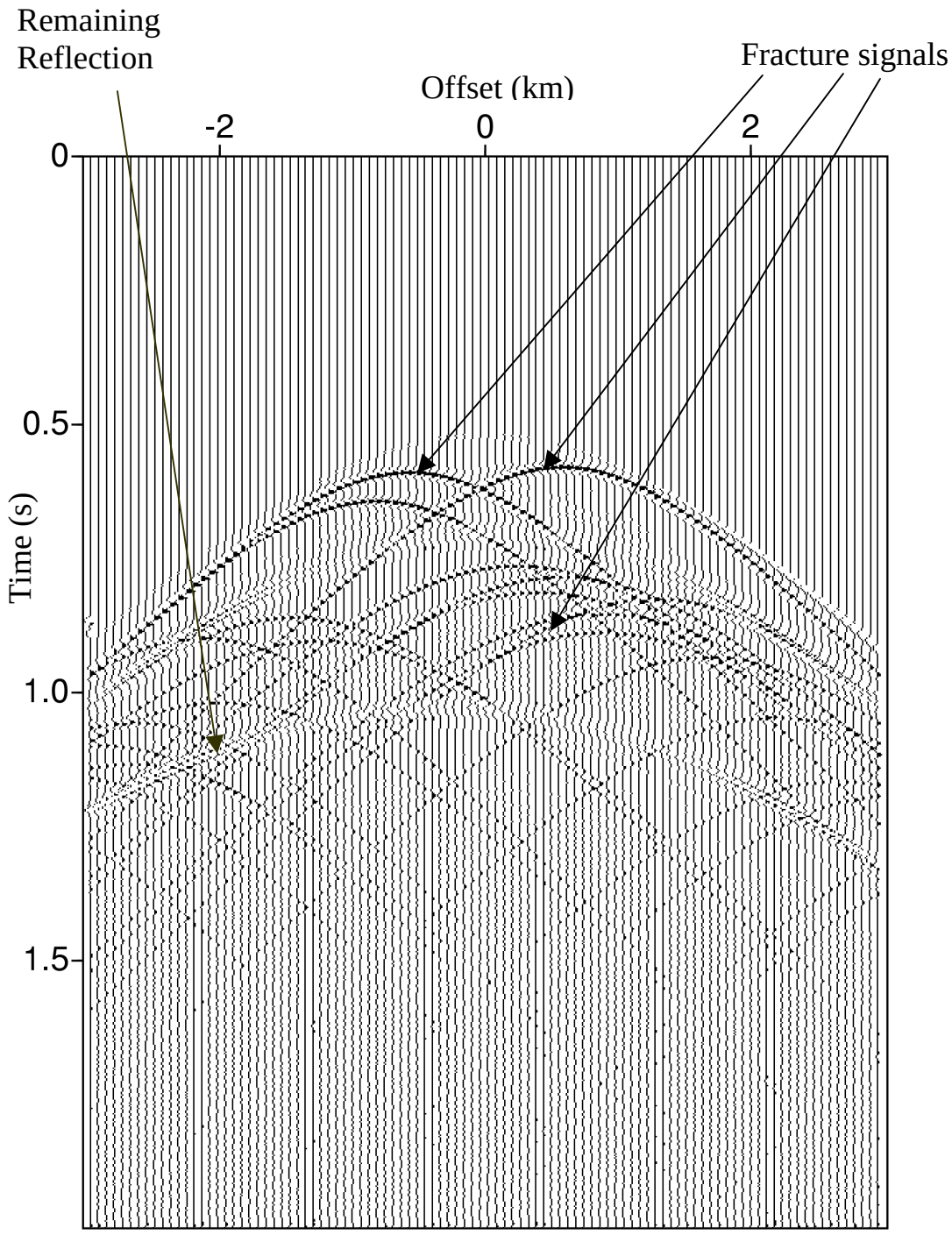

Figure 13: Shot gather after applying Harlan's (1984) filter.
The fracture signals are preserved with some added noise artifacts. The bottom reflection is not removed completely because of its steep dip.

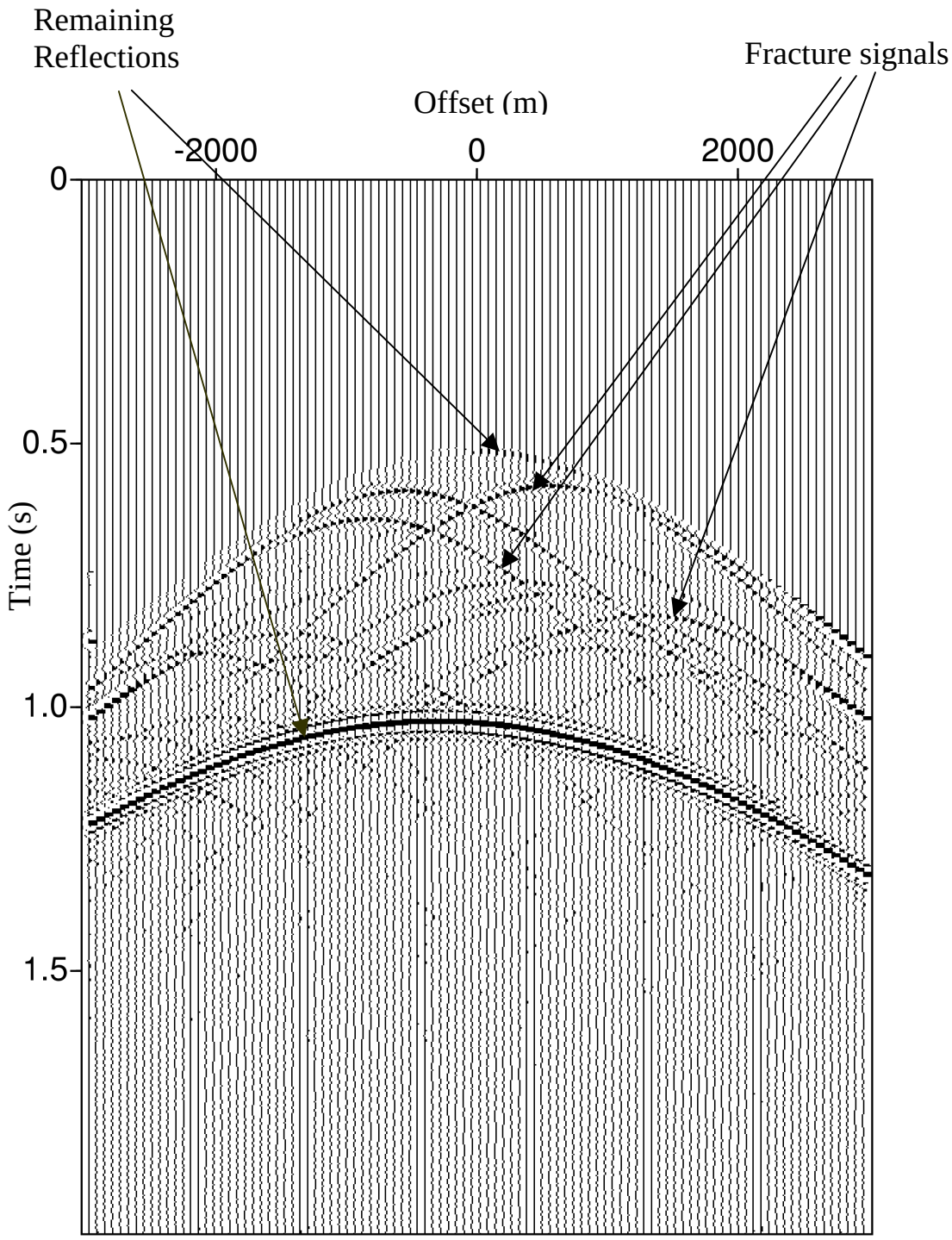

Figure 14: Shot gather after Radon filtering.
The bottom reflector is weakened but still strongly present.

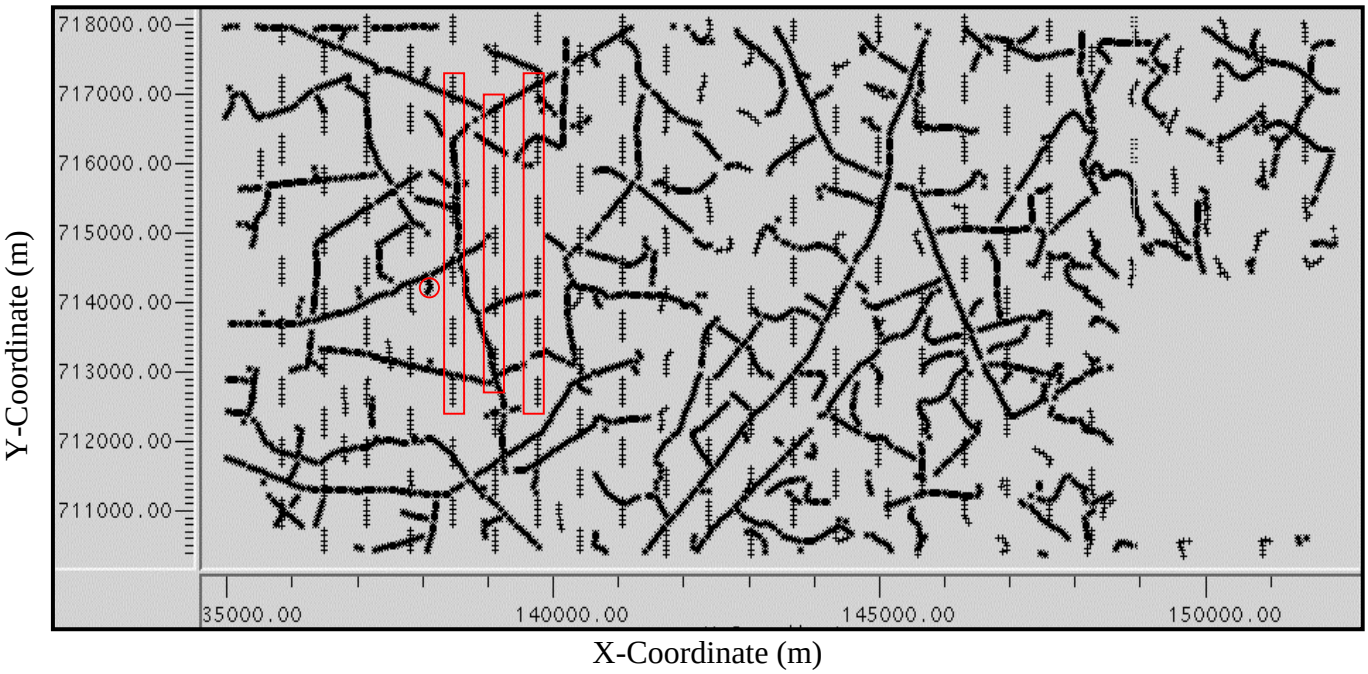

Figure 15: Survey geometry for 3D data set.
Geophones are almost following a regular brick pattern. Shots are only placed along roads. X-and Y-coordinates are state plane coordinates. The red boxes and circles define receivers and shot used to evaluate the workflows.

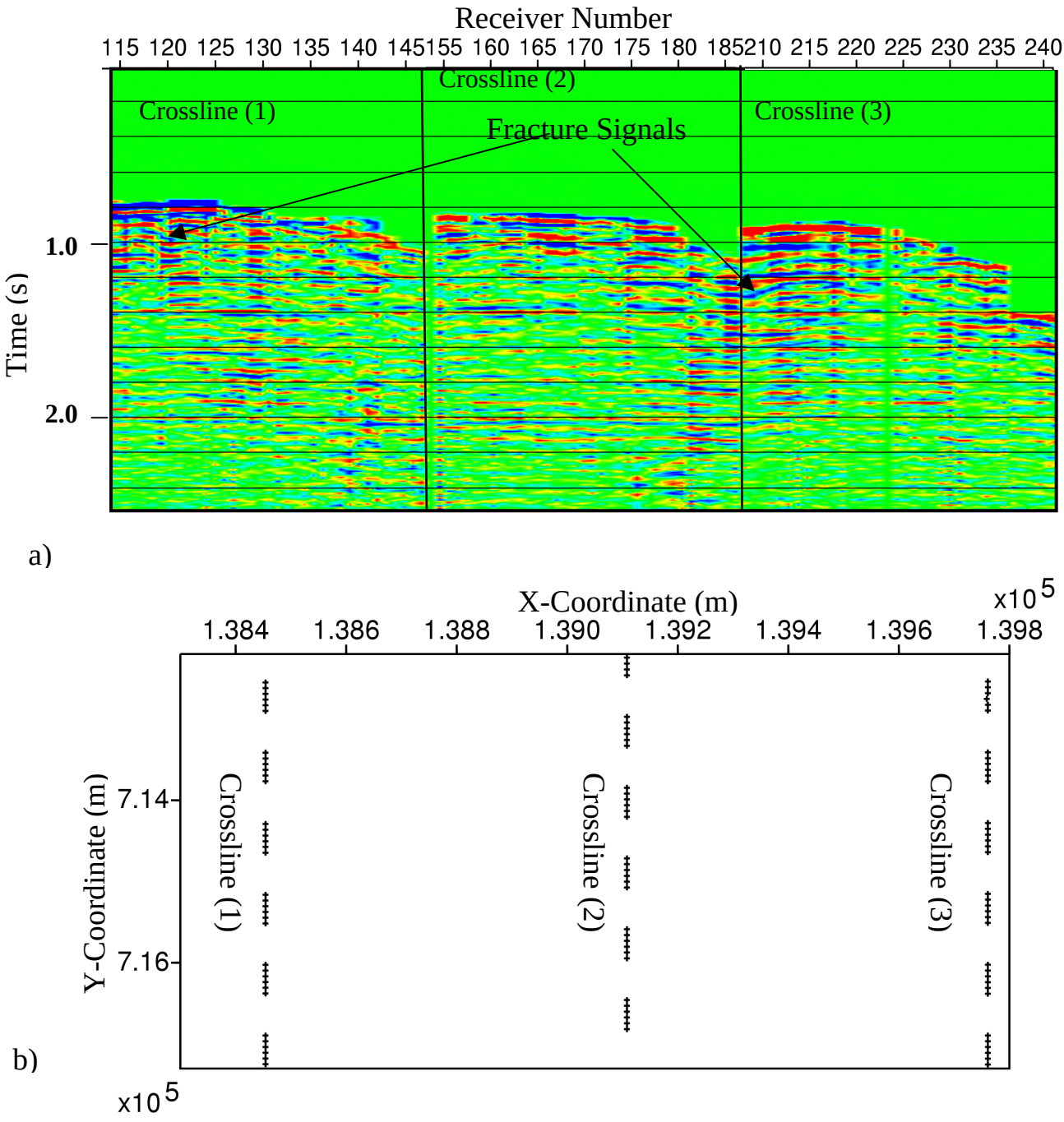

Figure 16: Shot gather from 3D data
a)Traces are sorted in their receiver inline number and receiver crossline number. In this shot gather, three receiver cross lines (1), (2), and (3) are present. The data is NMO corrected and most of the reflection hyperbolas are almost flat. Fracture signals are present as S-shape events. b) Star marks are showing the position of receiver.

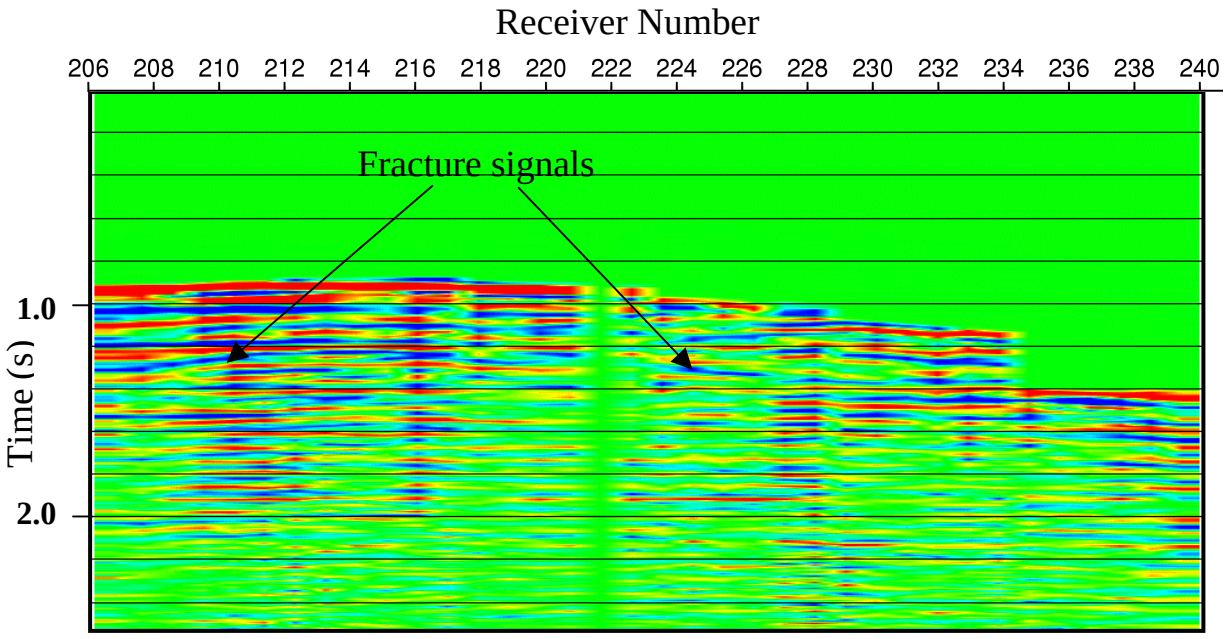

Figure 17: Shot gather from crossline (3).
Fracture signals are observed. Reflection hyperbolas are almost flat after NMO correction.

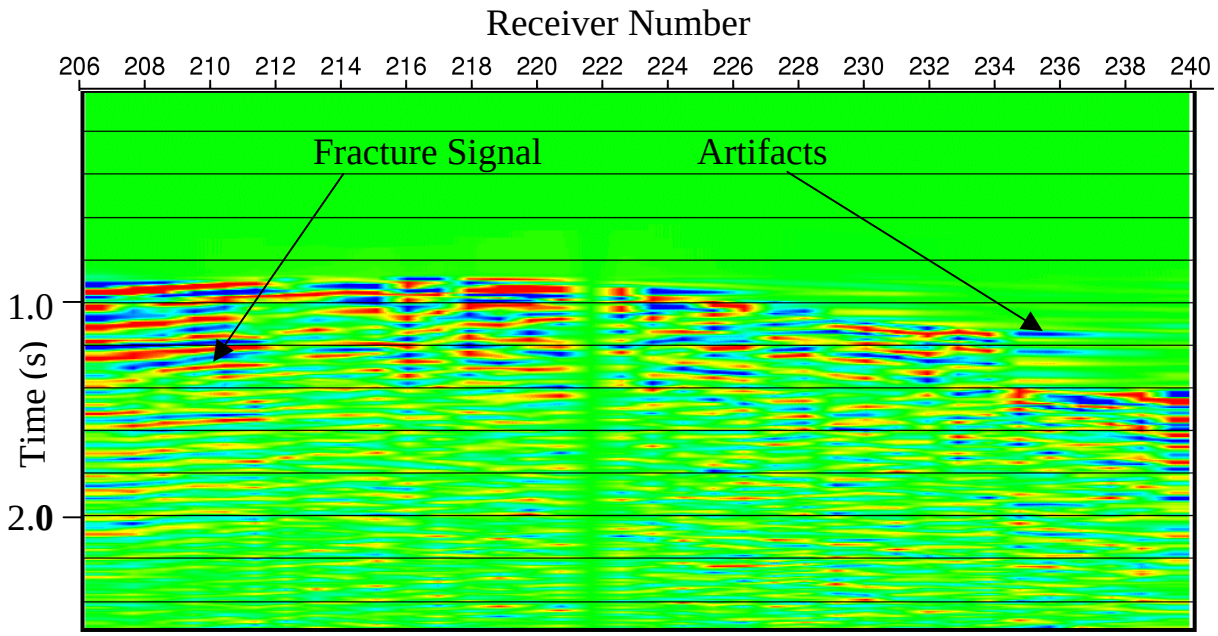

Figure 18: Crossline (3) after dip filtering in F-K domain.
Fracture signals are preserved though flat part of these signals are removed due to dip filtering.

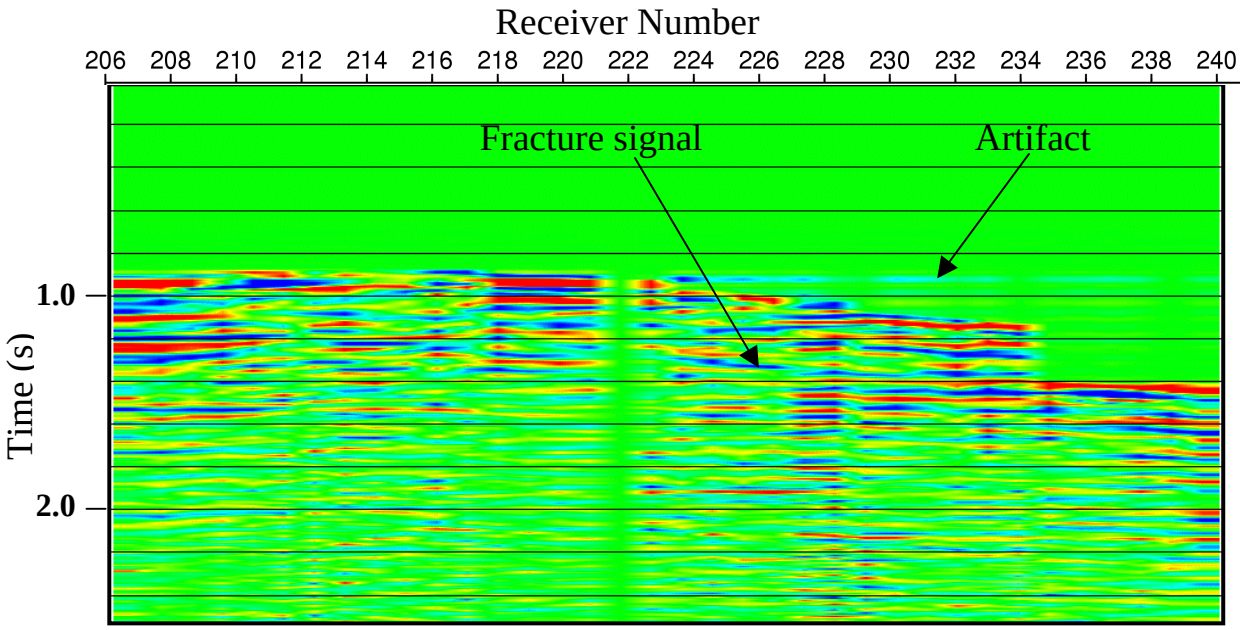

Figure 19: Crossline (3) after Eigenvector filtering.

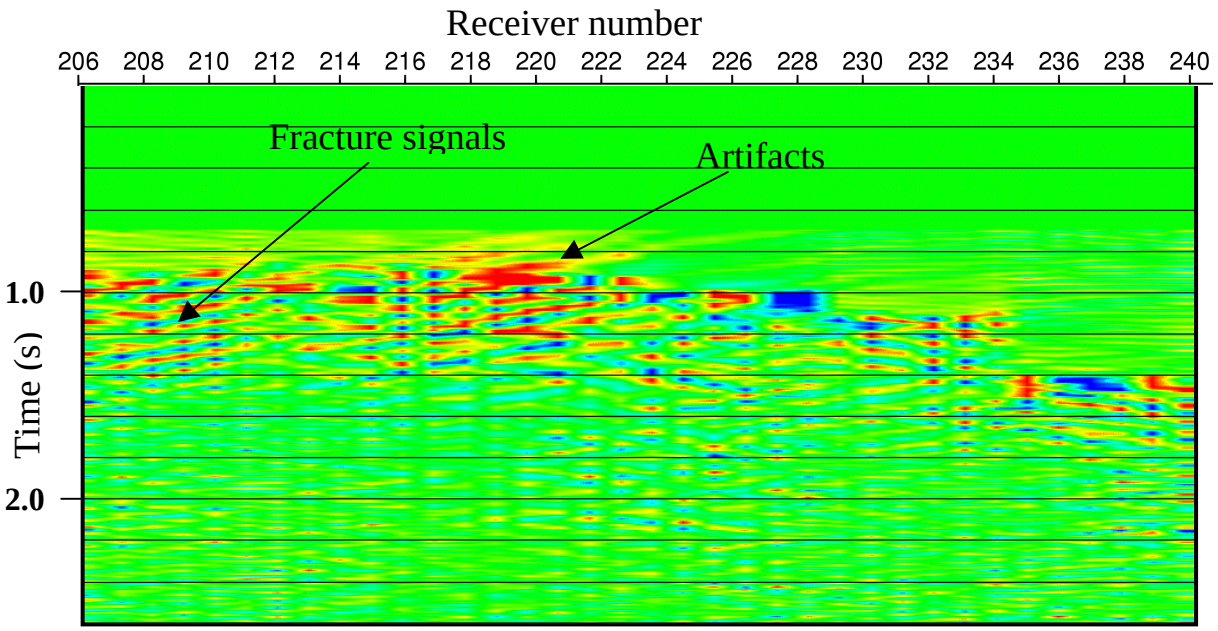

Figure 20: Crossline (3) after applying Radon Filter

Appendices

A: Fractures Signature

Lawrence Berkeley National Laboratory conducted numerical experiments on discrete fracture zones to understand their seismic response (Daley, et al., 2002). Fractures are modeled as finite length columns with equal normal and tangential stiffness representing gas-filled fractures or joints. Theses fracture stiffnesses result in anisotropic perturbations of elastic parameters which are computed using the method of Coates and Schoenberg (1995).

A 5-layer model (Figure A1) was developed with two sets of discrete fractures in the Measaverde formation from the San Juan Basin. Four long, compliant joints with a stiffness of $8x10^8$ Pa/m spanned the entire Mesaverde unit, while 107 short, stiff fractures with a stiffness value of $8x10^9$ Pa/m were limited to the Cliffhouse Sandstone member. The large fractures are 650 m long with a spacing of 600 m, while the short fractures are 60 m long with 21 m spacing. The background velocity model was built from wireline data. Seismic surface shot gathers were generated using a point source with a 50 Hz Ricker wavelet and 38 sensors with 60 m spacing.

Figure A2 shows snapshots of the propagating wavefields at 400 ms time through the model with and without fractures. The snapshots for these models differ greatly. As expected, we clearly see the transmitted (downgoing) and reflected waves (upgoing) from the interfaces without any fractures. But in the presence of fractures, we observe additional events corresponding to scattered energy, prominent P-to-S conversions ("V" shapes), and fracture-tip diffractions.

The effect of the fractures on surface seismic observations is shown in Figure A3 which compares seismograms for the vertical velocity component for models with and without the fracture sets. The discrete fractures cause additional coherent events. Strongly coherent events (fracture-tip diffractions) are caused by the large and discrete fractures. The small, clustered fractured zones give rise to multiple scattering manifested by ringing, coda-like events.

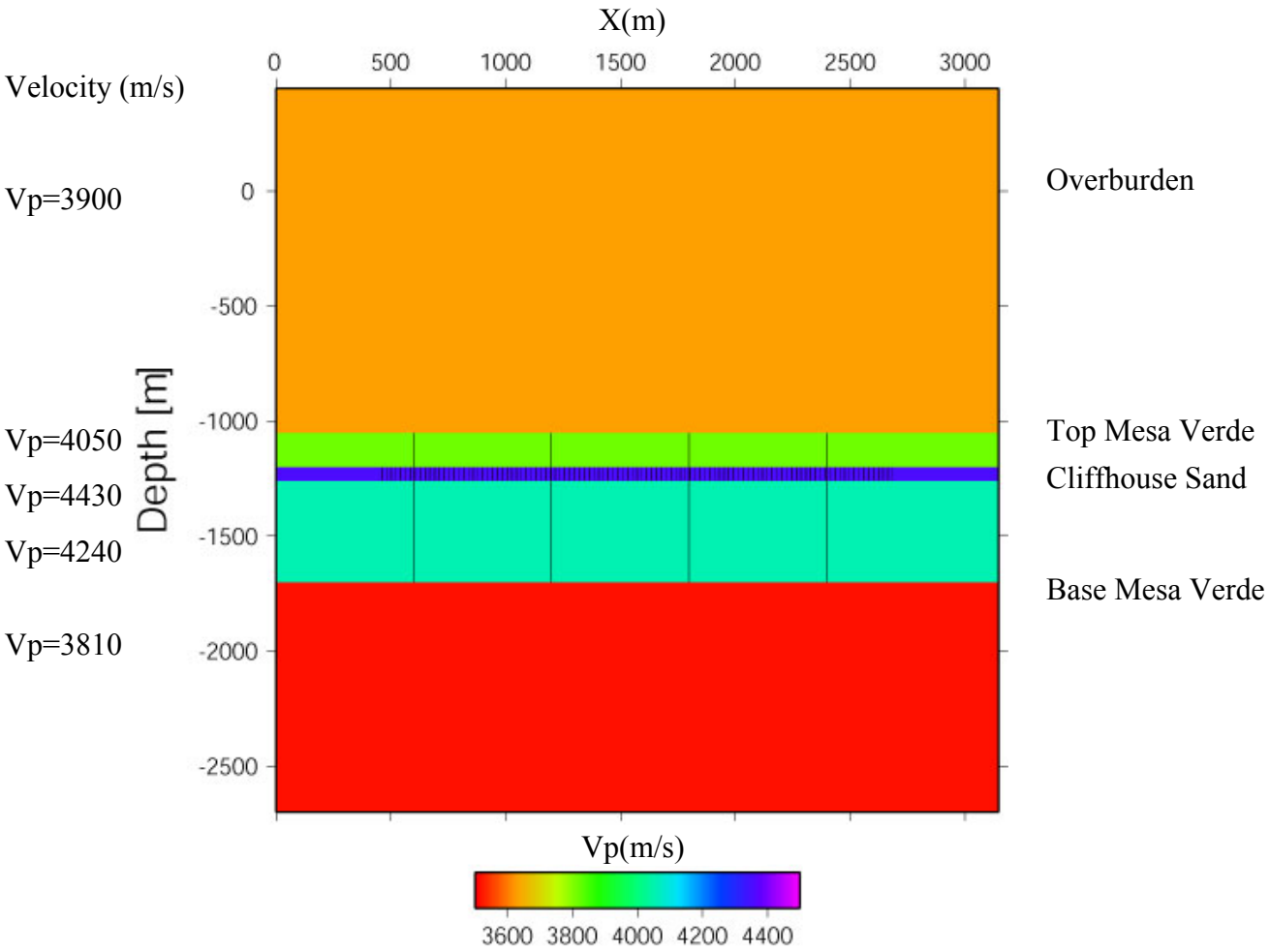

Figure A1: Subsurface model (Daley, et al., 2002)
Five layer subsurface model used to generate fracture responses in a surface seismic section. The model imitates the Mesaverde formation from San Juan Basin. There are two sets of fractures in the model. Four long, compliant fractures span the Mesa Verde unit, while 107 short, stiff fractures are confined to the Cliffhouse sand.

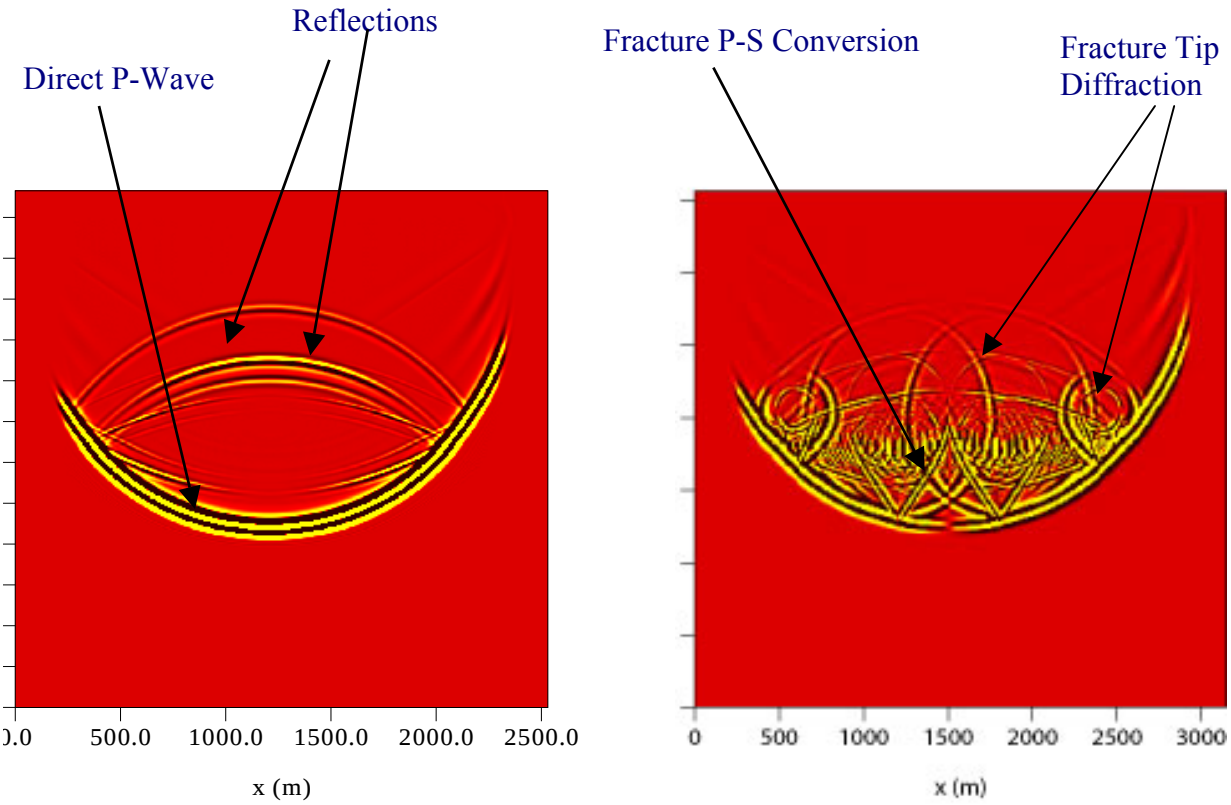

Figure A2: Wavefield propagating through the subsurface model at 400 ms (Daley et al., 2002)
a) Wavefield propagating through the model without fractures. Direct P-wave and reflections from layer boundaries can be observed. b) Wavefield propagating through the model with fractures. Strong scattering and complex wavefield are evident due to the fractures. Fractures are producing off-tip diffractions and P-to-S conversion ("V" shapes).

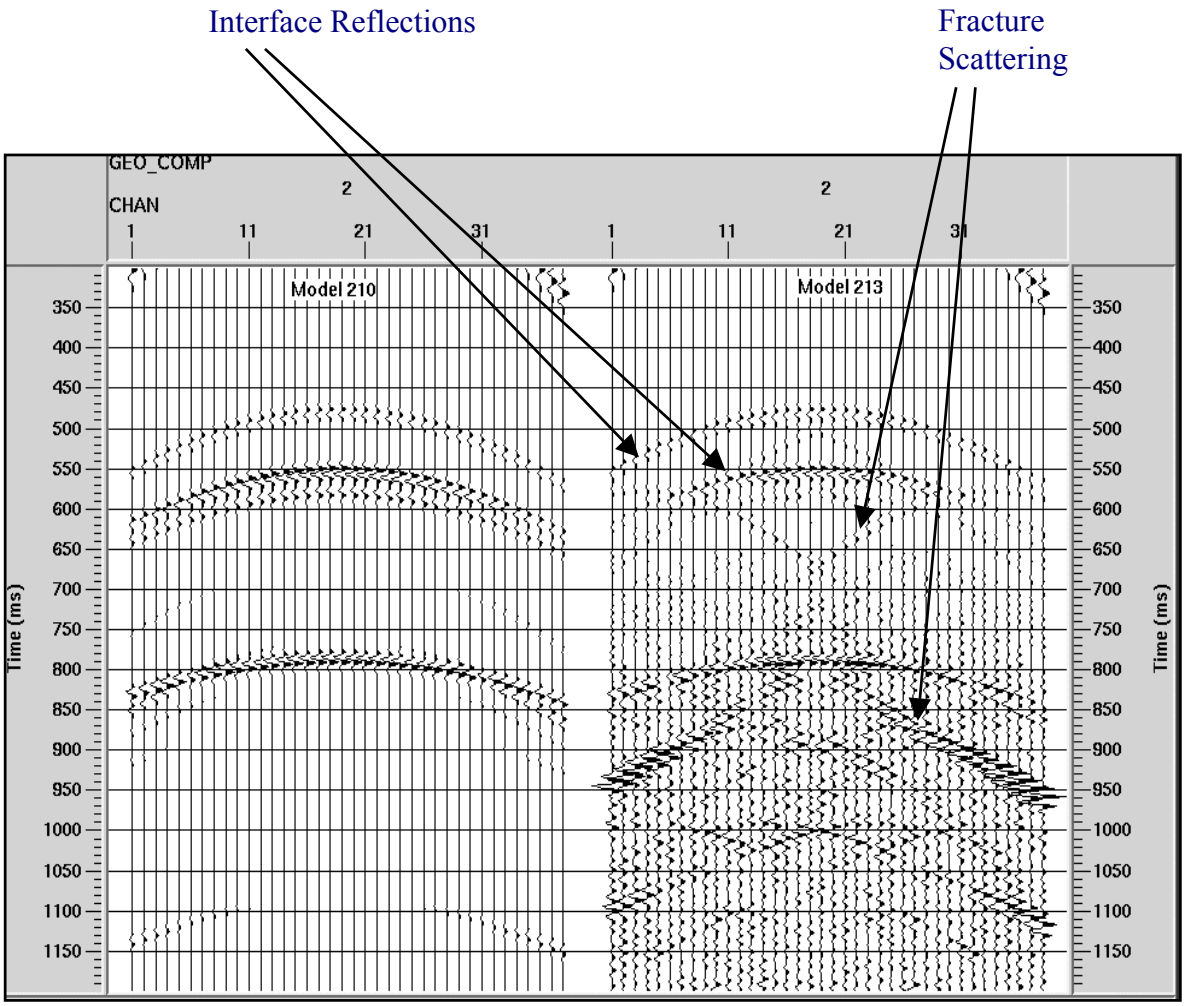

a) **b)**

Figure A3: Response of the subsurface model in surface seismic data (Daley et al., 2002)

a) Shot gather in absence of subsurface fractures. The seismic traces are for velocity particle with the vertical component at true relative amplitude. Only interface reflections are observed. b) Shot gather in presence of subsurface fractures. Coherent fracture events are observed. The incoherent energy (coda) is present due to the ringing arrivals from multiple scattering caused by small, stiff fractures.

B: Moveout delay of diffractions

Diffractions have always larger moveout delay than reflections. The diffraction traveltime curve for a scatter (Figure B1) can be derived as follows (Sheriff and Geldart, 1995),

$t_d = (1/V)\{(h^2 + a^2)1/2 + [(x - a)^2 + h^2]\}$

$\approx (2h/V) + (a^2/2Vh) + (x - a)^2/2Vh$

If $2h/V = t_o$ (Zero offset time)

$\approx t_o + (2a^2 - 2ax + x^2)/2Vh$

If $x^2/4Vh = \Delta t_n$ (reflection moveout delay)

$\approx t_o + 2\,\Delta t_n + a(a - x)/Vh$

Here, V is the seismic velocity of the media.

It is apparent that diffractions have larger moveout delay than reflections.

If scatterer lies below the shot point, above equation becomes

$t_d = t_o + 2\,\Delta t_n$ which shows that the diffractor moveout delay is twice the moveout delay of a reflector at the same depth.

Figure B2 presents the travel time curve for a reflector at depth h and a diffractor at depth h below the shot point.

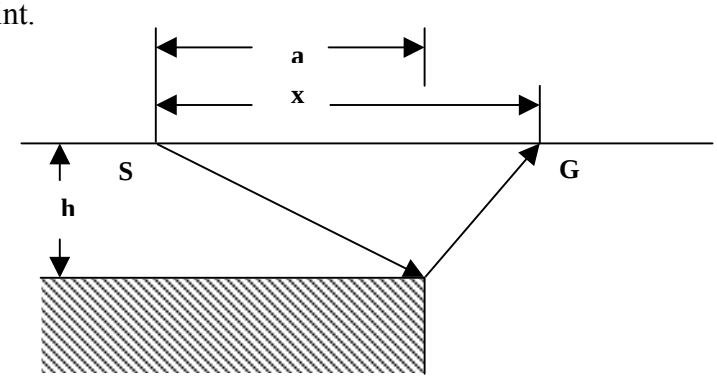

Figure B1: Scatterer is at diastase a from shot point S. G is the position of the receiver. Seismic velocity in the medium is V.

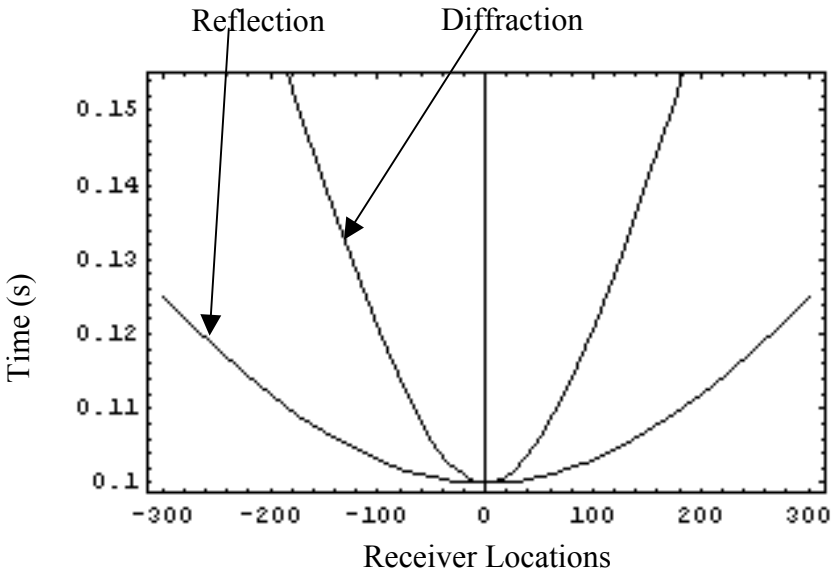

Figure B2: Travel time curves of a reflector and a scatterer at depth h. The diffractor is located below the shot point. The diffraction has more moveout delay than the reflection.

C: Response of a dipping bed after NMO correction

After NMO correction, steeply dipping beds may become S-shaped which might which could be mistaken for fracture signals.

Figure C1 shows the travel time curve and it's NMO corrected response for a dipping bed at 40^0 with a vertical distance between shot point and the bed of 50 m. It is obvious from Figure C1 that NMO corrected travel-time curve becomes S-shaped..

Figure C2 shows travel time curve and it's NMO corrected response for a bed dipping at 40^0 with the shot point placed at 200 m vertical distance from the bed. The NMO corrected curve is almost a straight line and can be distinguished from fracture signals easily.

In case of steeply dipping reflection interface at shallow depth, hence, it may be advantageous to apply DMO corrections prior to any of the proposed processing schemes to enhance fracture signals.

In another study, we computed a shot gather for a dipping bed at 27^0 with vertical distance between the shot point and the bed of 725 m. The subsurface velocity is 4500 m.

Figure C3 shows the seismogram for offsets between –995 and 995 m. Figures C4-C6 show NMO corrected sections obtained with the true NMO velocity, a 10% lower NMO velocity and a 10% higher NMO velocity. In all three cases, the reflection hyperbola turned into an almost straight lines which could be distinguished easily from fracture signals. Horizon boundaries in our study area are not very steeply dipping as illustrated by the NMO velocities picked from the field data (Figure D1). We are confident that the fracture signals are not attributed to dipping beds. But dipping beds are not flattened

perfectly by NMO correction, and hence, they may not be removed completely from the data using the proposed workflows. Residual events from dipping layers might be interpreted as fracture signals.

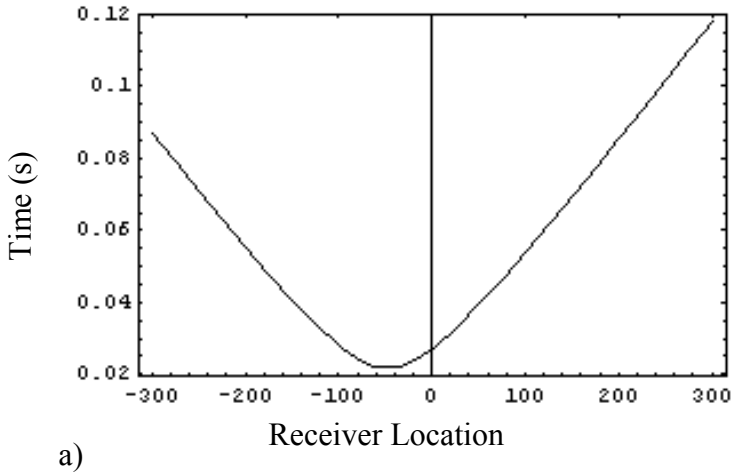

a)

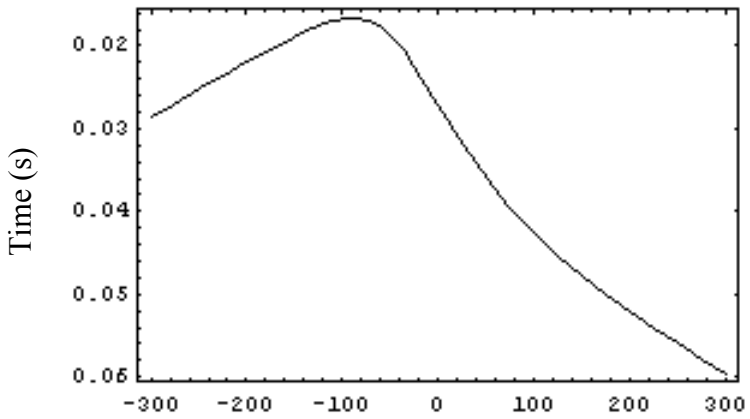

b)

Figure C1: Travel time curve and NMO corrected response of a bed dipping at 40^0 at a depth 50 m.
Figure a) shows the travel time curve of the reflector. Figure b) shows the NMO corrected curve which is not a linear event and could be mistaken for a fracture signals.

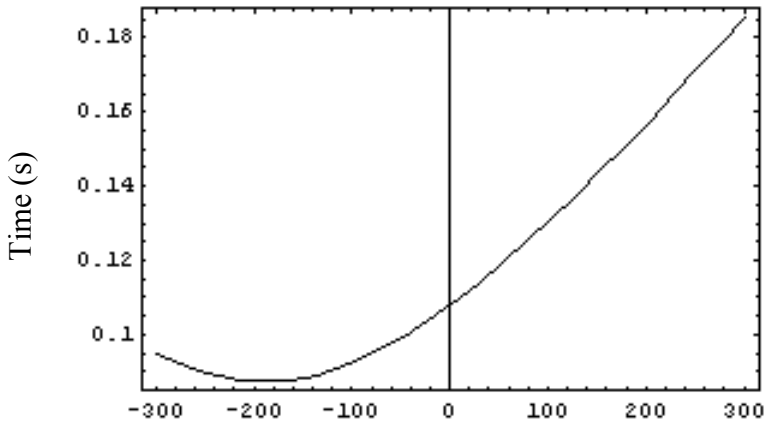

a)

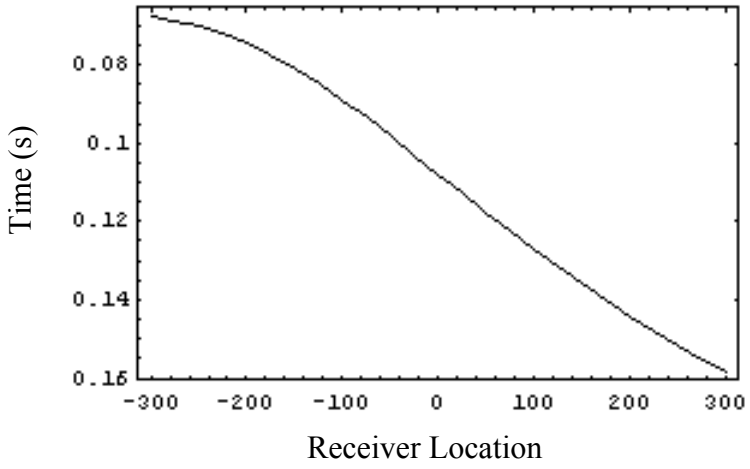

b)

Figure C2: Travel time curve and NMO corrected response of a bed dipping at 40^0 at a depth 200 m.
Figure a) shows the travel time curve of the reflector. Figure b) shows the NMO corrected curve. This is almost a straight line which is nearly linear and should be distinguished from fracture signals.

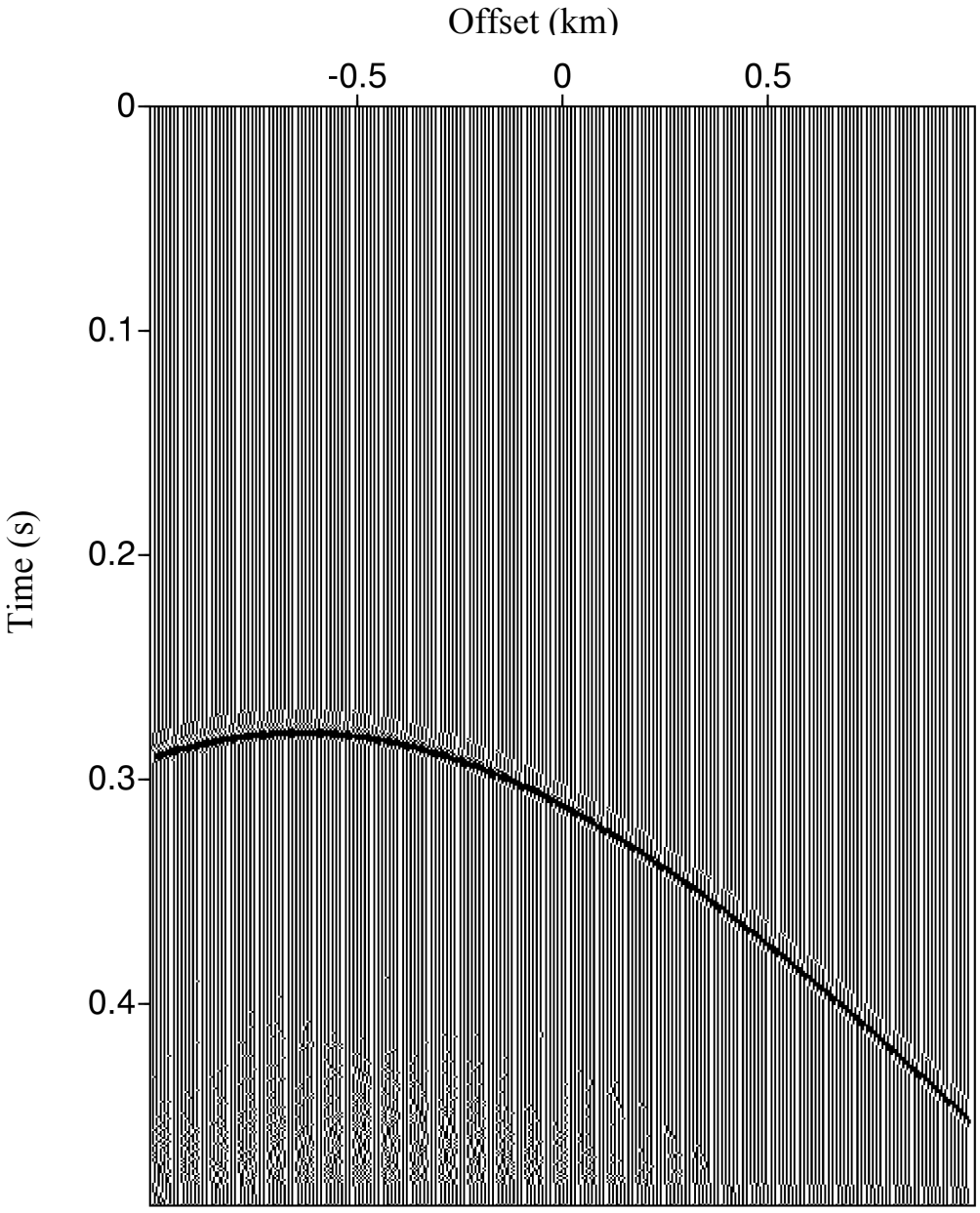

Figure C3: Shot gather of the seismic response of a bed dipping at 27^0.

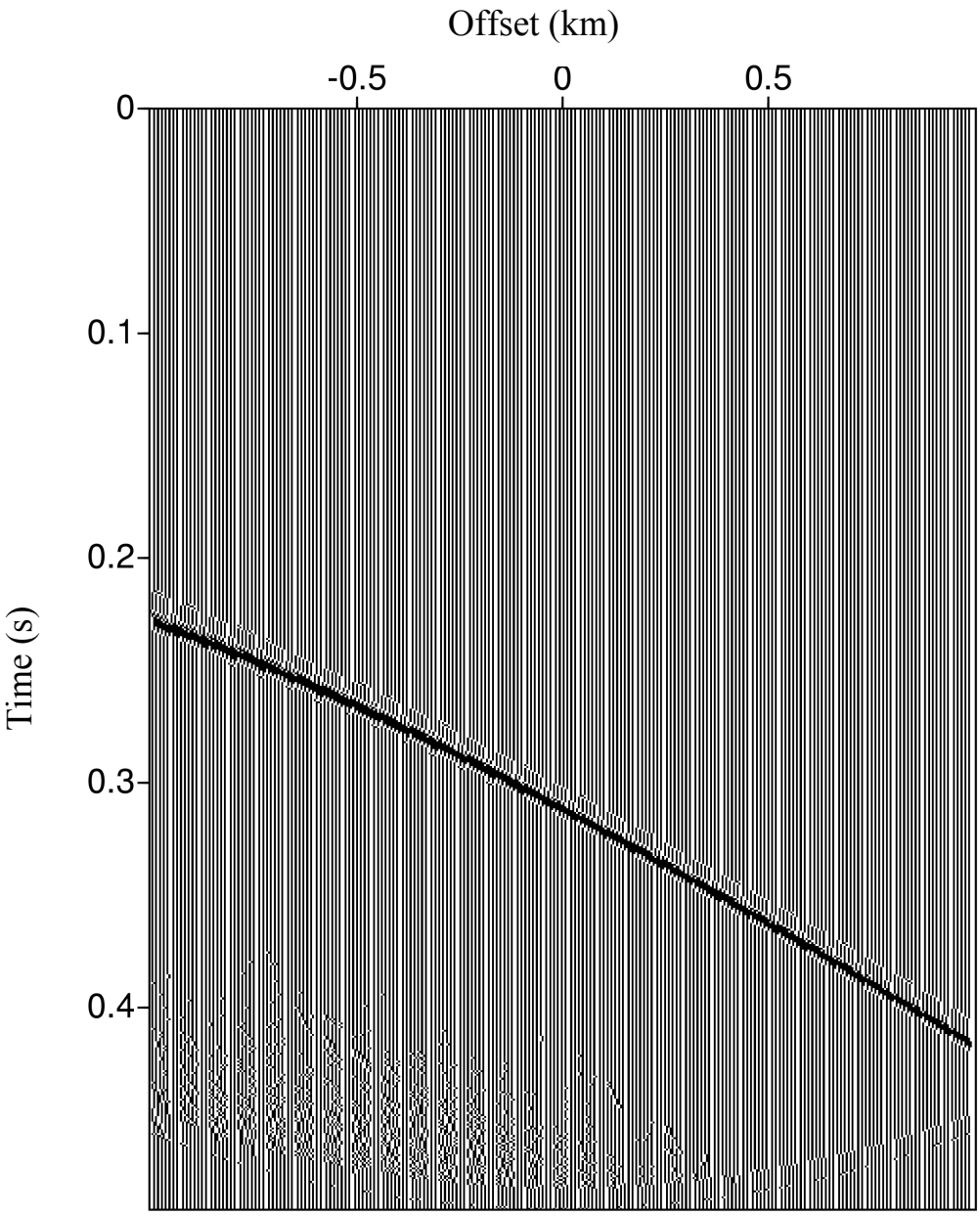

Figure C4: Shot gather after NMO-correction with true NMO velocity

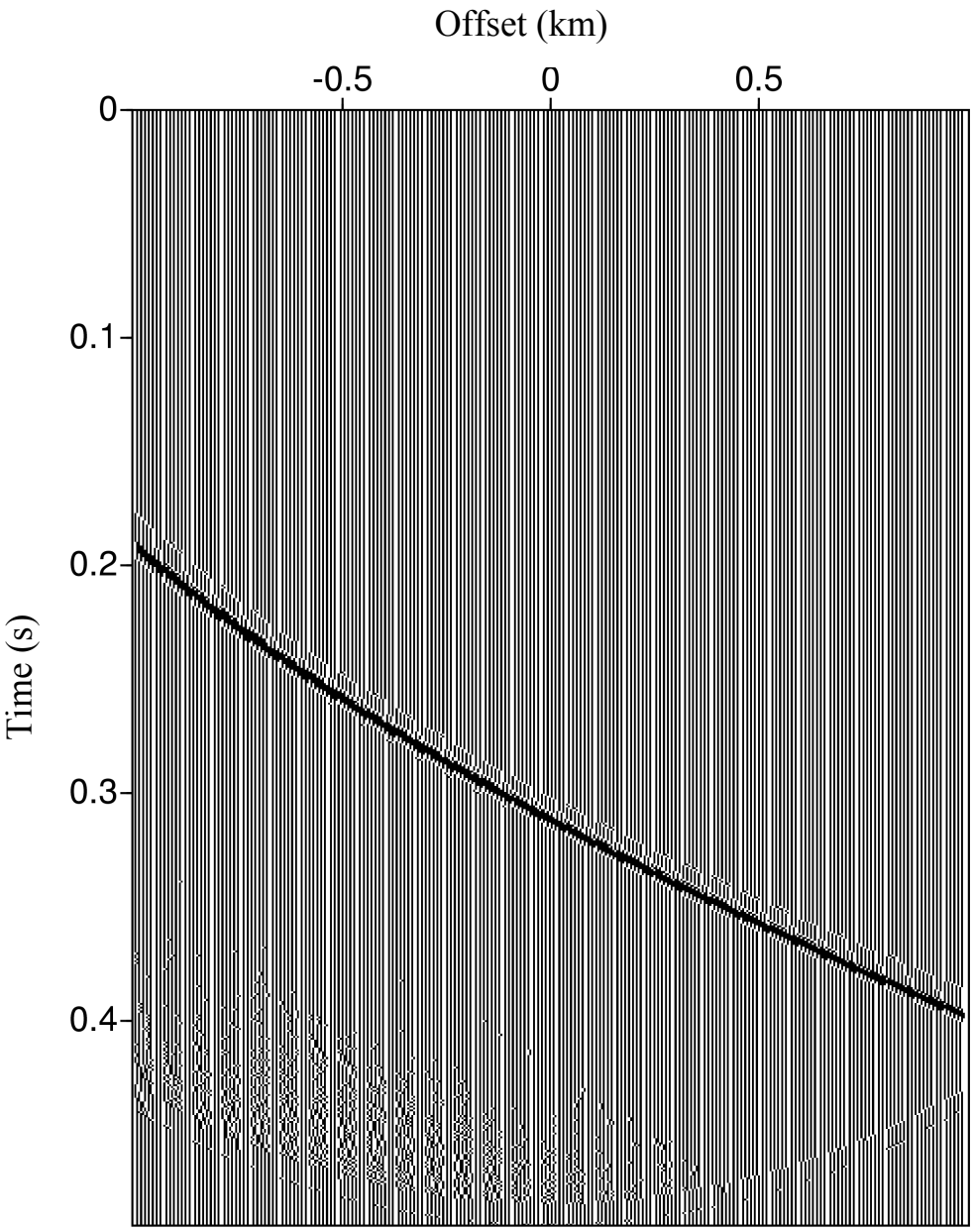

Figure C5: Shot gather after NMO correction with 10% lower NMO velocity

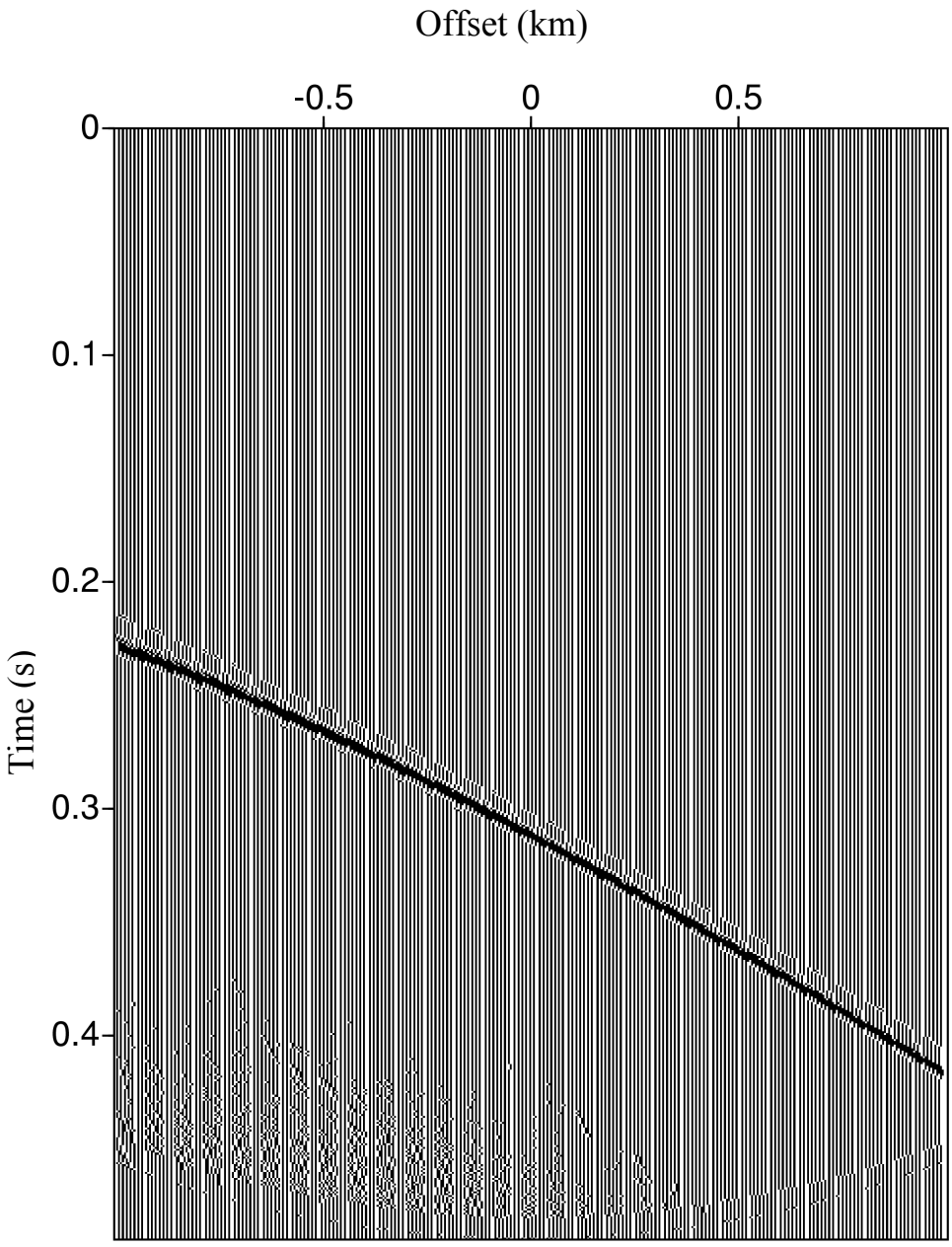

Figure C6: Shot gather after NMO correction with 10% higher NMO velocity

D: Dip of the beds in the study area

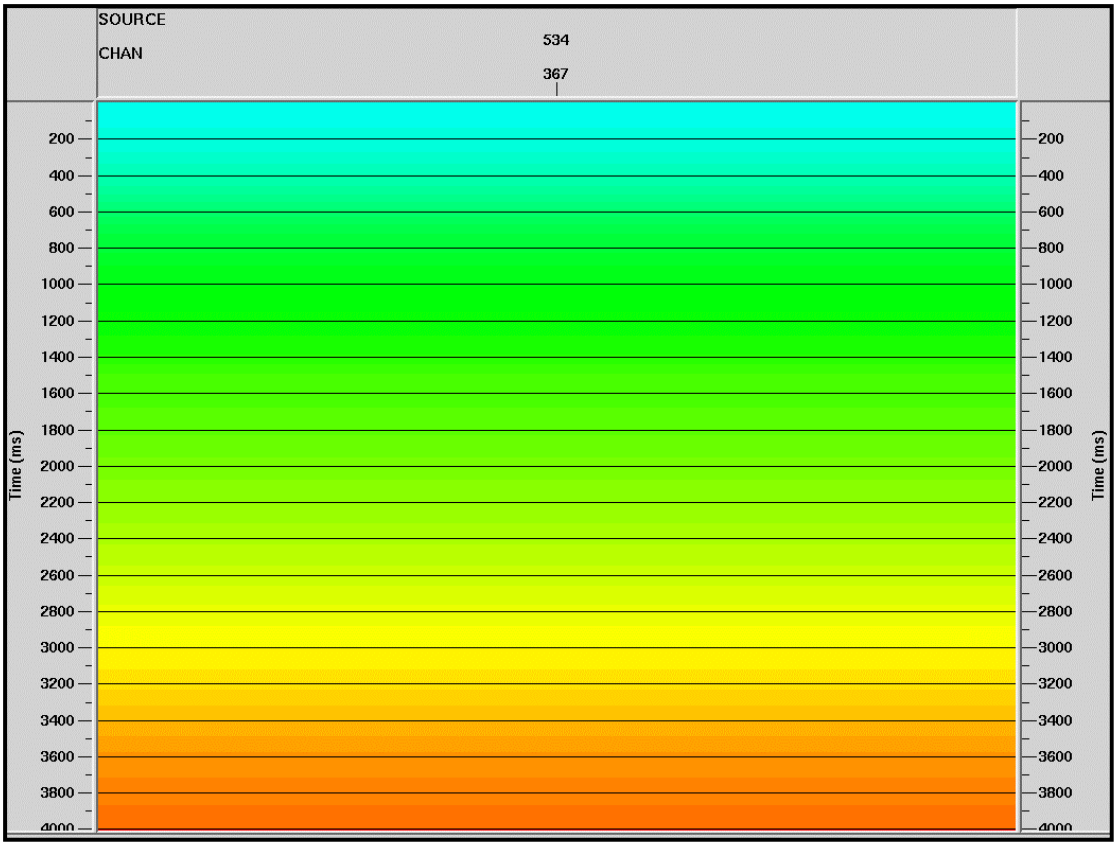

Figure D1: Stacking velocities from study area.
The stacking velocities exhibit very little lateral velocity variations which indicates very gently dipping layers. Well confirms this finding.

VITA

REESHIDEV BANSAL

EDUCATION

- **Phd, Geophysics**
  University of Texas at Austin from Fall, 2003
- **M. S., Geophysics,** MAY 2003.
- **B. Sc. (Honors), Geological Sciences,** 2000. Completed 1st year of **Master in Exploration Geophysics**, 2001.
  Indian Institute of Technology, Kharagpur, India.

RESEARCH

Discrimination and Enhancement of Fracture Signals on Surface Seismic Data. Manuscript to be submitted to **Geophysics**

PUBLICATIONS

- R. Bansal, M. G. Imhof, and T. Daley. Seismic Characterization of Fractures in a Naturally Fractured Gas Reservoir: 72nd Annual Internat. Mtg., Soc. Expl. Geophys, Expanded Abstracts 2002.
- R. Bansal, M. G. Imhof, Enhancement of Surface Seismic Fracture Signals: 73rd Annual Internat. Mtg., Soc. Expl. Geophys, Expanded Abstracts 2003, Submitted

RELATED EXPERIENCES

- **Graduate Research Assistant,** Department of Geological Sciences, August, 2001-May, 03.
- **Courses** – Seismic Prospecting, Geophysical Signal Processing, Computer Applications in Geophysics, Seismic Migration, Continuum Mechanics, Wave Propagation in Solids, Seismic Stratigraphy, Computational Seismology, Perturbation Methods.
- Mapped the geology of Aangool, India as fieldwork project in undergraduate course.